

A Waveguide High Order Mode Reflectometer for the Large Hadron Collider Beam-pipe

T. Kroyer

Abstract

For good operation of CERN's Large Hadron Collider, it is of the utmost importance that the beam-screen is perfectly straight and free of any obstacle larger than the size of a pinhead. During the installation procedure, however, there is a non-negligible probability of permanent deformation or simply that some forgotten object stays inside. In this case it would very useful to have a tool to detect such obstacles both during assembly and possibly later in situ without having to reopen the vacuum. In this project the feasibility of a reflectometer using synthetic pulses of high order waveguide modes was examined. The characteristics of the beam-pipe and the beam-vacuum interconnects were studied experimentally and the results compared to theoretical models. For the signal attenuation found it should be possible to cover a few hundred meters at room temperature and, if present estimations hold, half an arc (1250m) at 20K. Digital signal processing was used to extract the original reflection profile on dispersion-affected measured and simulated data. Finally the methods were checked on a 50m test track.



Diplomarbeit

A Waveguide High Order Mode Reflectometer for the Large Hadron Collider Beam-pipe

ausgeführt zum Zwecke der Erlangung des akademischen Grades eines
Diplom-Ingenieurs unter der Leitung von

Arpad L. Scholtz

E389

Institut für Nachrichtentechnik und Hochfrequenztechnik

eingereicht an der Technischen Universität Wien
Fakultät für Elektrotechnik und Informationstechnik

von

Thomas Kroyer

9726048

Mitterweg 632, A-7201 Neudörf

Wien, im April 2003

Abstract

For good operation of CERN's Large Hadron Collider, it is of the utmost importance that the beam-screen is perfectly straight and free of any obstacle larger than the size of a pinhead. During the installation procedure, however, there is a non-negligible probability of permanent deformation or simply that some forgotten object stays inside. In this case it would very useful to have a tool to detect such obstacles both during assembly and possibly later in situ without having to reopen the vacuum.

In this project the feasibility of a reflectometer using synthetic pulses of high order waveguide modes was examined. The characteristics of the beam-pipe and the beam-vacuum interconnects were studied experimentally and the results compared to theoretical models. For the signal attenuation found it should be possible to cover a few hundred meters at room temperature and, if present estimations hold, half an arc (1250m) at 20K. Digital signal processing was used to extract the original reflection profile on dispersion-affected measured and simulated data. Finally the methods were checked on a 50m test track.

Contents

1	Introduction	1
1.1	A brief introduction to CERN	1
1.2	The LHC	1
1.2.1	The beam-screen	2
1.3	The concept of the reflectometer	2
1.3.1	Discussed methods for detecting obstacles	3
1.3.2	Possible realizations	4
2	The calibration procedure	5
2.1	Calibration in a 50 Ω coaxial system	5
2.2	Waveguide calibration for an S-band waveguide	6
2.2.1	Definition of the calibration kit	6
2.2.2	Test of the calibration's sensitivity	6
2.2.3	Perturbations inserted into the waveguide	8
2.3	Gating	9
2.4	Conducting irises	10
2.5	Waveguide calibration for a C-band waveguide	12
2.5.1	Calibration in spite of badly estimated cut-off frequencies	13
2.6	Waveguide calibration on the beam-pipe	14
3	Resonator measurements with the beam-pipe	15
3.1	The cut-off frequencies	15
3.2	The attenuation measurement	17
3.2.1	The TM mode	18
3.2.2	The TE modes	19
3.3	Check on a rectangular C-band waveguide	22
3.4	Attenuation at 20K	24
4	The interconnects	29
4.1	Resonator measurements	30
4.2	Measurements in reflection mode	31
4.3	Examination of multiple reflections with BNC cables	34
5	Signal processing	36
5.1	The Fourier transform	36
5.1.1	Windowing	36
5.1.2	Dispersion compensation	39

5.1.3	Attenuation compensation	40
5.2	Simulations	41
5.2.1	Multiple reflections by the interconnects	41
5.2.2	Mode mixing	44
6	Measurements on the “50m” test track	48
6.1	Performance of the actual signal processing	49
6.2	Attenuation	52
6.3	The interconnects	54
6.4	The TE modes	56
6.5	Mode mixing	57
6.6	Power scattering from the slots	58
7	Conclusion	61
A	Derivation of the formula for the cut-off frequency	62
B	Characteristics of the network analysers used	63
C	Picture gallery	64
	Bibliography	69
	Acknowledgements	71

Chapter 1

Introduction

1.1 A brief introduction to CERN

After the destructions of World War II, European nuclear physics was in a very bad state. Seizing the suggestion of the French physicist Louis de Broglie, the *Conseil Européen pour la Recherche Nucléaire*, or *European Organisation for Nuclear Research* was formally established with 11 member states in 1954. For the site of the CERN laboratory complex the quiet village Meyrin a few kilometers outside Geneva close to the French border was chosen.

Today CERN has 20 member states and works in close collaboration with many non-member states like the U.S., Russia, India or Japan. Today the focus of activities concentrates on the Large Hadron Collider (LHC), which will become operational in 2007. In addition to particle physics there are many spin-offs in other technologies, the most famous being the World Wide Web, that was developed at CERN in 1990-91.

1.2 The LHC

To push the frontiers of physics further out, collisions at higher and higher energies have to be studied. Up to the end of 2000 the Large Electron-Positron Collider (LEP) was in service, opening up an important new discovery domain. With a length of nearly 27km it was the world's largest particle accelerator, achieving beam energies of up to 100GeV. After exploiting the LEP for 11 years, it was decided to shut it down to make place for the next generation particle accelerator, the Large Hadron Collider (fig. 1.1). To avoid costly civil engineering work, the existing LEP tunnel about 100m underground will be reused for the installation of the new machine. The LHC is scheduled to become operational in 2007.

The LHC's proton beams will be accelerated to an energy of 7TeV, which is 70 times higher than in LEP. To keep the beam on track, powerful superconducting magnets producing fields up to 8T, cooled with super fluid helium are necessary. In figure C.1 the cross-section of an LHC cold arc is shown. The entire assembly is under high vacuum. In the very center are the two beam-pipes embedded in the dipole magnets.



Figure 1.1: The ring of LHC. The CERN labs are located at the left close to the point where the two larger rings intersect. The dotted line is the border between Switzerland and France. Note the Geneva International Airport at the bottom of the picture for scale

1.2.1 The beam-screen

The beam-pipe consists of two parts, an outer ultra low-temperature part, the cold bore (1.9K), and the beam-screen (20K) in the center (fig 1.2). The latter is destined to shield the superconducting magnets from synchrotron radiation emitted from the beam. The beam-screen is manufactured with specially developed stainless steel. On the inner surface there is a $75\mu\text{m}$ copper coating to minimize the impedance seen by the beam-induced image currents [9].

The beam-screen is covered with 8 rows of axial pumping slots to allow the evacuation of residual gas. On one side the inner surface is covered with saw-teeth like corrugations to capture the synchrotron radiation. Due to the manufacturing process a small welding strip will stay on the side opposite to the corrugations. They can be seen in figure C.8(b) as well as the welding strip. On the outside of the beam-screen two stainless steel cooling tubes are welded to ensure an operating temperature between 5 and 20K.

1.3 The concept of the reflectometer

In the past some strange objects have been found in particle accelerators, e.g. beer bottles, metal rules, cleaning towels or simply contact fingers of a badly installed interconnect. A reliable means to detect and localize such obstacles would be highly desirable, preferably without the need to break the vacuum.

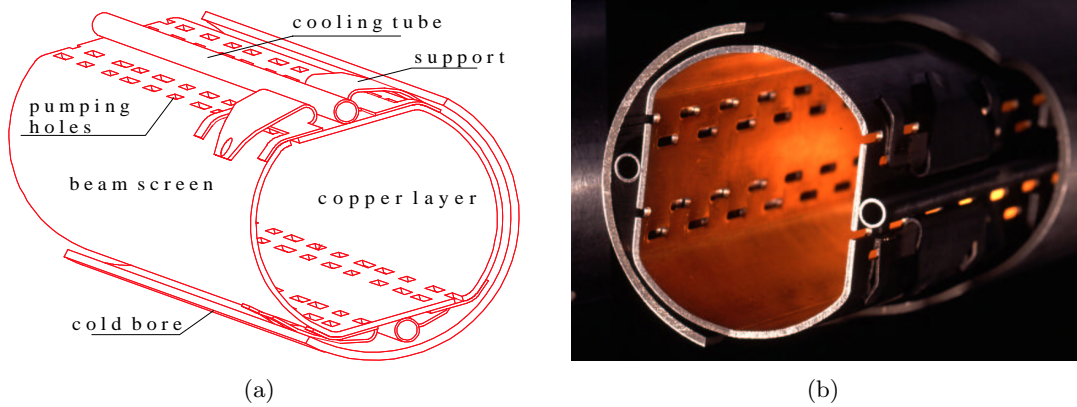


Figure 1.2: The LHC beam-screen with the surrounding cold bore, the pumping slots and the cooling tubes

1.3.1 Discussed methods for detecting obstacles

Various approaches have been discussed for detecting and locating such obstacles, in particular

- Laser reflectometry
- Ultrasonic pulse-echo
- FMCW¹ “radar”
- Real time pulse reflectometry
- Synthetic pulse reflectometry

While the first two methods failed immediately due to limitations in range, the ultrasonic detection is additionally constrained to operation with some gas present in the beam-pipe. The other three made it to the finals.

FMCW. In principle obstacle detection on the beam-pipe seems possible using a kind of FMCW radar system. In reality however it soon becomes clear that whoever has to build such a system must start from first principles. Most of the front-end measurement equipment, including mixers with very good image suppression, is not commercially available for the huge dynamic range we need to cover. Development would thus be very costly in time, material and manpower.

Real time pulse reflectometry. In many civilian and military aviation applications real time pulse reflectometry is used. The dynamic ranges reached may be very large. This is possible by increasing gain for far-away targets to compensate for free-space attenuation. In the beam-pipe however we have to cope with dispersion that is not present in the applications cited above. Additionally moving target detection is much easier than looking for a static target on the beam-pipe in presence of noise and interference.

¹Frequency Modulated Continuous Wave

Synthetic pulse reflectometry. This method is similar to one presented above, with one important difference: The measurements are not done in the time but in the frequency domain. A certain range is scanned, measuring the response for each frequency point. Then the time domain data is calculated by doing an inverse Fourier transform. This technique offers four major advantages:

- A state of the art vector network analyser (VNA) can be used, so no front-end measurement equipment has to be developed. All the RF parameters can be very well controlled, which gives good reproducibility
- Waveguide calibration for the beam-pipe is possible, which potentially allows to compensate effects of feed cables, connectors and adapters
- Waveguide dispersion can be corrected numerically on the frequency domain data
- We can take profit from the high dynamic range available for frequency domain measurements

1.3.2 Possible realizations

The most interesting parts of LHC to be examined by a reflectometer are the cold arcs, since they are very hard to access after cool-down. Breaking the vacuum and opening an arc in the case of a problem would be an enormous effort. Since cold arcs are very homogeneous and present very little attenuation for an electromagnetic wave, especially at low temperature, this field of application looks quite promising. For the other parts of LHC an operation would be very difficult due to the changes in beam screen profile and the beam instrumentation.

In this project, the feasibility of two different versions of the reflectometer was examined:

- **The baseline plan:** During assembly, sections of say 100m length are to be checked before sealing the beam-pipe. The measurement would be done at room temperature with air in the beam-pipe by branching some kind of connector directly on one end.
- **The full version** should allow in-situ measurements in the LHC. Coupling to the beam-pipe should utilize some kind of button type pick-up. Since it is only possible to install those couplers at the end of an arc, the spatial range would have to be much larger. A detection range of at least half an arc's length (1250m) in reflection would be necessary to cover an entire arc by looking from both sides.

For the actual state of the project consult [the LHC reflectometer page!](http://www.cern.ch/tkroyer/reflec/)

(<http://www.cern.ch/tkroyer/reflec/>)

Chapter 2

The calibration procedure

In this chapter we will have a look onto questions of how the vector network analyzer (VNA) calibration is done, and why it is important. To get good measurement results of any kind, it is of utmost importance to do a careful and exact calibration. As in all measurements, systematic errors alter the results. In time domain reflectometry (TDR) these are directivity of the internal directional coupler, source match, reflection tracking, transmission tracking, and isolation [6]. Doing calibration allows the VNA to adapt its internal error model to the environment used and subsequently to remove the error mathematically. To perform a reflection (s_{11}) calibration, the VNA needs to measure the frequency response of three well-defined standards. In the coaxial technique the choice of preference is load, short and open circuit. Using waveguides, this must be altered, as an open circuit is not well realisable. Normally, a load and two off-set shorts are used. This fulfills the condition that the three standards be well separated in amplitude (load-short) and phase (short1-short2).

2.1 Calibration in a 50Ω coaxial system

To get some experience, calibration was done on the HP 8753 for a simple 50Ω system. We used type N 50Ω connectors and an ordinary HP calibration kit with the standards open, short and load. Then the calibration was tested with the aim to find an appropriate criterion to verify waveguide calibration. The most obvious possibility was to check in the logarithmic magnitude representation if s_{11} is close to 1 for pure reactances, e.g. an open transmission line, and sufficiently small (-40dB) for an adapted load [7]. Even more convenient than the log magnitude representation is the Smith Chart. All you have to do is check whether s_{11} stays right in the center for an adapted charge and on the outer circle ($|s_{11}| = 1$) for pure reactances. By connecting open or shorted transmission lines, s_{11} should swirl clockwise towards the center of the Smith Chart. If s_{11} crosses the outer circle, as it does for active components, there must be something wrong. This simple and unambiguous criterion will be used to judge further calibrations. There is still another possibility: by using the VNA's time domain capability, it can be checked if there is a reflection at $t = 0s$ when some component, e.g. a transmission line, is connected. This initial reflection was observed to be some 2 orders of magnitude below the emitted synthetic pulse.

To complete the coaxial training, some tests were performed employing the VNA's windowing and averaging functions. A shorted line was observed in time domain while

reducing the IF bandwidth from 3kHz to 10Hz. Close to the reflected pulse the side lobes of the windowing function are clearly visible. Going further away, the curve falls towards the noise level.

2.2 Waveguide calibration for an S-band waveguide

After having made first experiences with standard coaxial lines, we had to get acquainted with waveguides. In the following experiments we used an aluminium S-band waveguide with the dimensions $a = 72mm$ and $b = a/2 = 36mm$. Due to the lack of a real transmission line, a 20dB directional coupler of 103cm length was used in its place. For calibration we had a fixed load and a sliding short at our disposition.

2.2.1 Definition of the calibration kit

Following [6] we defined a new Cal(ibration) Kit with a load and two offset shorts. The free lengths of the short standards were set to $\lambda_0/8$ and $3\lambda_0/8$, calculated with $\lambda_0 = c_0/f$ for $f = 2.944GHz$. These values give free lengths of $l_1 = 12.7mm$ and $l_2 = 38.2mm$, corresponding to free delays of 42.5 and 128ps, respectively. In general f should be somewhere in the center of the frequency range where the standard is used.

It is important that the longest standard be shorter than $\lambda_H/2$, λ_H designating the guided wavelength, for the highest frequency in the frequency range. If this condition is ignored, the calibration becomes singular when $l_2 = \frac{\lambda_H}{2}$ and produces an error that looks like a kind of resonance at this frequency.

The VNA has to get the some other information to be able to set up its mathematical model. These are the cut-off frequencies of the first and the second TE mode, $f_{c1} = 2.082GHz$ and $f_{c2} = 2f_{c1} = 4.164GHz$. These two cut-off frequencies constitute the limits of the maximum frequency span for a given waveguide in mono-mode operation. For the offset loss 0Ω was chosen, and the system impedance was set to $Z_0 = 50\Omega$.

The frequency range was chosen to be approximately $1.2f_c < f < 1.9f_c$, that is $2.3GHz < f < 4GHz$, for two reasons: first, it is recommended in the literature [1]. Second, as we noticed later, no good calibration is possible for a larger frequency span, because its behaviour close to cut-off gets very nasty. We think that this is caused by the fact that the VNA corrects for the waveguide dispersion using the formula $Delay = c_0/(f\sqrt{1 - (f_c/f)^2})$ [6]. However, this is just an approximation. Close to the cut-off the discrepancy becomes very large. The physical reason for this is that close to the cut-off the losses due to surface resistance are no more negligible.

These frequency limits were checked by an uncalibrated measurement of s_{21} showing that the attenuation of the S-band waveguide used stays almost constant between 2.25 and 4GHz. To be sure that the higher modes are well attenuated at the reference plane, we added a 12cm piece of waveguide after the coax adapter.

The Cal-Kit obtained was used for all subsequent measurements and calibrations in the S-band.

2.2.2 Test of the calibration's sensitivity

With the Calibration Kit defined above we tried to get a reasonably good calibration. It passed the Smith Chart criterion rather well. For pure reactances the curve deviated

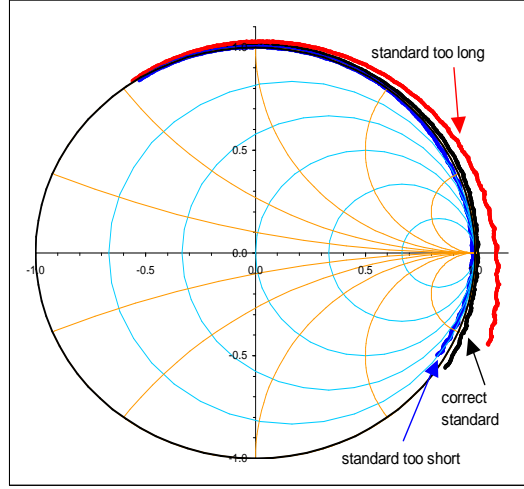


Figure 2.1: Smith Chart plot of a purely reactive load for three different calibrations

only slightly from the unity circle. Then we connected the adaptor plus waveguide to the directional coupler, our “transmission line”, terminated by an adapted load. In time domain, we found that the reflections from the matched load at $t = 0s$ were in the region of 10mUnits in linear scale. This seems to be not so bad.

Influence of the higher modes exited in the adaptor. In the next test the reference plane was set directly to the end of the coax adaptor. This plane just being some 4.2cm from the opening of the inner coax conductor, we were led to the assumption that at the reference plane there could still be found lots of higher waveguide modes. The visual control in the Smith chart did not reveal much aberration. Connecting the adaptor to the directional coupler showed equally that the time domain response was almost identical to the one measured before. So the higher modes seem to be sufficiently attenuated not to influence the calibration. There is no need to use a piece of waveguide after the coax adaptor. The following tests were all performed with the adaptor only.

Influence of handling. In this test the waveguide equipment was assembled with the greatest care. All mechanical connections were done accurately and solidly screwed together. Again, no significant changes were observed. This meant that very careful assembly was not necessary.

Influence of the precision of the calibration standards. Here we physically changed the length of the calibration standard short1 by 10% to $l = 14.058mm$. Even after this very significant modification the time domain response hardly changes. For pure reactances s_{11} no longer stays on the unit circle, in the log magnitude representation the trace drifts towards higher values compared to the original data, with an error growing with frequency up to 0.90dB.

We used for testing our short-circuit, varying its length between $l = 0$ and $l = \lambda_0/2$. The error is maximum for a short-circuit at the mean of the two frequencies used for calibration, corresponding to $l = 26mm$. The response is much better than the uncalibrated result, and not so far off the result obtained by correct calibration. In the

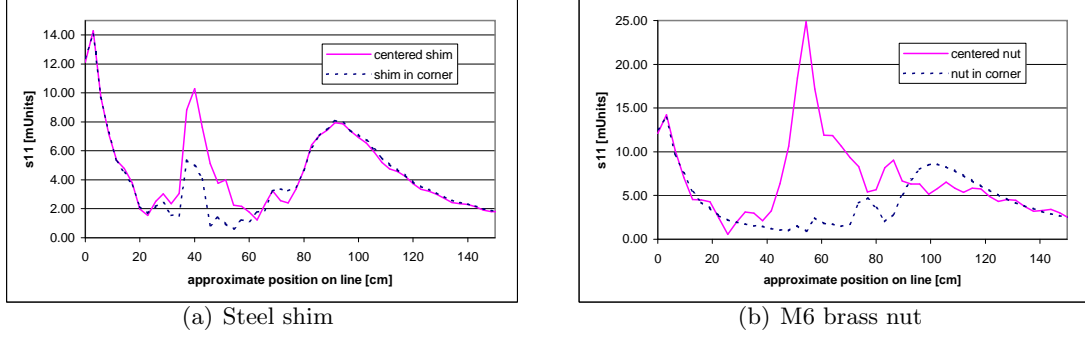


Figure 2.2: Reflections from metallic objects in an S-band waveguide

time domain the amplitude of the initial pulse is 14.3mUnits (compared to 8.6mUnits for the correct calibrated version, maximum at $t = 104ps$) and the maximum is shifted towards negative time by 850ps.

To get a better feeling, we did this kind of test once more with different parameters: The length of the short1 standard was decreased by 2% to 12.524mm. This precision ($\pm 0.25mm$) seems to be feasible in practice. As expected, the frequency response stayed below the curve obtained by correct calibration by 0.56dB maximum. Here we find an amplitude of 10.2mUnits of the initial pulse in the time domain, while its maximum is shifted to the right by 40ps. The Smith Chart criterion is illustrated for these three calibrations in fig. 2.1. Note that the curve drifts inwards or outwards in dependence of the sign of the length variation of the calibration standard.

We can therefore say that the calibration procedure is not very demanding in precision, minor variations of the standards do not cause large measurement errors.

2.2.3 Perturbations inserted into the waveguide

The following measurements were performed using the calibration described above. In the time domain we observed characteristic responses from

- Metallic objects
 1. 15mm steel nail, centered, standing, at $x = 100cm$
 2. 24mm diameter steel shim, centered, at $x = 75cm$, see fig. 2.2(a)
 3. 24mm diameter steel shim, in corner, at $x = 75cm$, see fig. 2.2(a)
 4. M6 brass nut, centered, at $x = 89cm$, see fig. 2.2(b)
 5. M6 brass nut, in corner, at $x = 89cm$, see fig. 2.2(b)
 6. 12mm steel screw, centered, standing, at $x = 100cm$
 7. 12mm steel screw, in corner, standing, at $x = 100cm$
- Dielectric objects
 1. M6 plastic nut, centered, at $x = 85cm$, see fig. 2.3(a)
 2. M6 plastic nut, in corner, at $x = 85cm$, see fig. 2.3(a)
 3. 23mm plastic screw, centered, standing, at $x = 95cm$, see fig. 2.3(b)

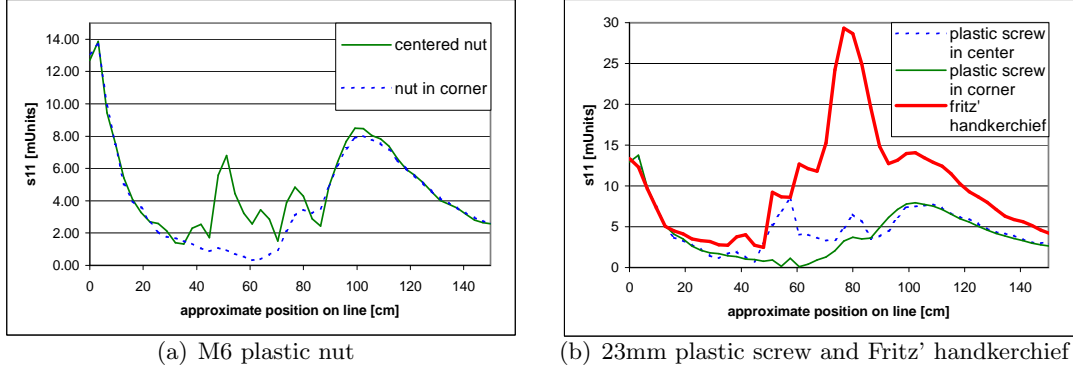


Figure 2.3: Reflections from dielectric objects in an S-band waveguide

4. 23mm plastic screw, in corner, standing, at $x = 95\text{cm}$, see fig. 2.3(b)
5. Fritz' handkerchief, recently used, at $x = 95\text{cm}$, see fig. 2.3(b)

Some of the obstacles are shown in C.2(a). The resolution of these images is not as good as on the VNA display, since the Fourier transform on the PC was not yet well implemented in this early stage of the project. The VNA apparently uses a quite elaborated FFT procedure¹. The horizontal axis represents either time or space on the waveguide, but the given values for the length are not very accurate.

2.3 Gating

To determine the impedance of a perturbation on the line, time domain gating can be used. This method can help to identify the nature of an obstacle as it allows to analyze a peak's spectrum. In the time domain, a region comprising the pulse of interest is "cut out" by a gating function. By setting the electrical delay to the position of the pulse, the response is shifted in time to the origin. Switching to the frequency domain, we can now see the reflection coefficient of this and only this pulse in the Smith chart, where we can directly read off the impedance values. This procedure depends heavily on the correct choice of the electrical delay. Almost any response can be obtained using a wrong delay.

In this experiment we met a 1.5m coaxial line at the VNA port and connected via a T-junction a 10Ω resist and another 1m of cable, its end left open. In time domain this should give quite a lot of reflections. After laying a gate of 5ns width over the desired pulse from the T-junction, we could neatly distinguish the parallel resistance of 10Ω and 50Ω giving 8.33Ω in the Smith Chart, as we measured 8.5Ω at 1.25Mhz. For higher frequencies the impedance drifts off towards the center.

To find the correct electrical delay, the first 1.5m coaxial line was short-circuited and the delay adjusted with regard to the Smith chart. The reflection coefficient was made to be as close as possible to -1. A cross-check with the line left open showed that in this case s_{11} was very close to +1.

To check the results obtained, the T-junction was then connected directly to the VNA port by a male to male junction. The curves found showed good agreement with

¹A chirp z-transform, as was later found out.

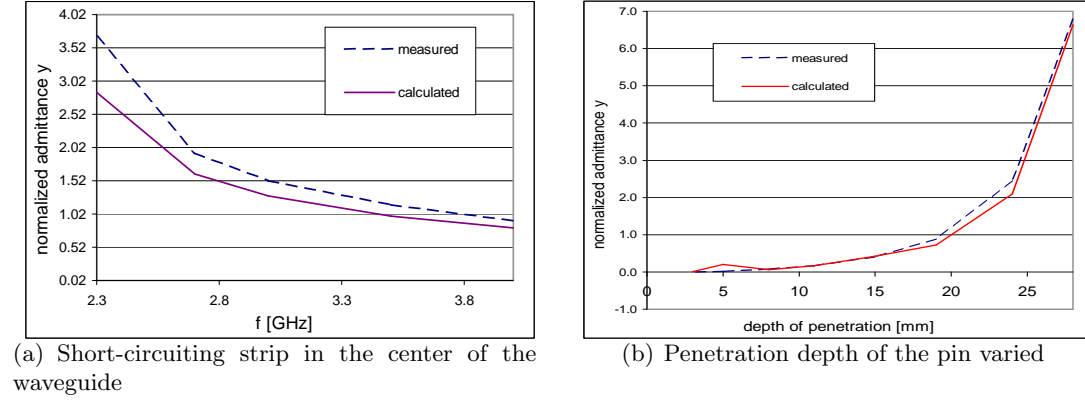


Figure 2.4: Admittance of copper pin in an S-band waveguide

those found by gating.

It was interesting to observe that if the open end is replaced by a matched load, the curves do not change much. This shows the effect of gating: The strong reflection of the open end did not significantly change the result, because it was far away in time or space.

2.4 Conducting irises

Inductive wire and copper strip. In this preliminary experiment we tested the attenuation of the TE_{10} mode by inserting a soldering wire at $x = 12\text{cm}$ in the center of the waveguide, parallel to the \vec{E} vector. The transmission coefficient s_{21} did not change much, while a strong reflection was observed.

Then we used a copper strip of 2mm width at the position $x = 0\text{cm}$ between the coax adaptor and the matched load. Even though we could see a very strong reflection the mode still propagates well beyond the copper strip. In the Smith chart we could read out a reactance of some 10nH @2.3GHz. The measured values were compared to those obtained from [1], given by

$$y = -jK_1\lambda_H/a, \quad (2.1)$$

with a designating the length of the longer side of the waveguide. K_1 is a scaling factor for the thickness of the wire or strip used that was read out from a chart in the textbook. As can be seen in figure 2.4(a) the measured values for the normalized admittance y , as always normalized with $y_{ref} = 50\Omega$, are within 20 to 30% of the calculations.

Inductive Copper strip reaching into the waveguide. To get closer to an actual problem in accelerators, namely contact fingers reaching into the waveguide, the copper strip was pulled out bit by bit. This case too is very well treated in [1]. For short pins or low frequencies the admittance is capacitive, while for longer pins or higher frequencies we should find inductive behaviour. On the left of figure 2.4(a) the relative admittance is plotted versus pin penetration depth for $f = 2.3\text{GHz}$. At this frequency the resonance length is larger than 28mm, this is why no distinct resonance can be observed.

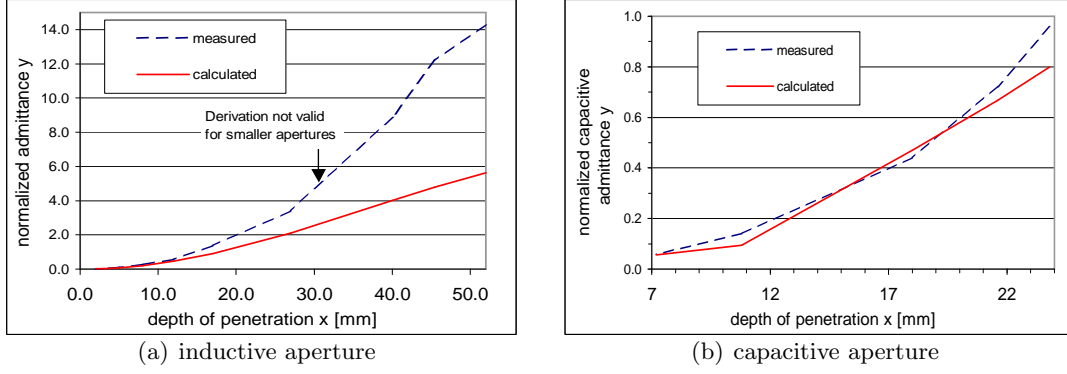


Figure 2.5: Admittance of an asymmetric aperture in an S-band waveguide

Inductive iris. An inductive iris was the next object considered. We simply put a copper foil between the flanges in the reference plane with its side parallel to the short side of the waveguide. By shifting its position the impedance can be changed, but it will always stay inductive as the magnetic field is constricted. In the literature we found just formula 2.2 that can be applied for symmetric apertures in [1].

$$y_{\text{symm}} = j \frac{\lambda_H}{a} \cot^2 \frac{\pi a'}{2a} \quad (2.2)$$

Here a' is the width of the aperture. To adapt the formula to our measurements we generalized it for asymmetric apertures

$$y_{\text{asymm}} = y_{\text{symm}} \frac{1 - \cos \frac{2\pi x}{a}}{2(1 - \cos \frac{\pi x}{a})} \quad (2.3)$$

with $x = \frac{a-a'}{2}$ being the penetration depth on either side for the symmetric aperture. For the asymmetric case the foil covers a width of $2x$ of the aperture. By Taylor series development of the correction factor (or an experienced look) it can be seen that it tends to 2 for little penetration depths of large apertures. The calculated values were corrected using the full formula. In figure 2.5(a) these values are compared to our measurement results. As the derivation is not valid for apertures smaller than $a/2$, the calculated values have not to be taken seriously.

Capacitive iris. We did much the same way as above with the capacity iris. To obtain the theoretical values, again a formula from [1] was used:

$$y = jB \frac{2a}{\lambda_H}, \quad (2.4)$$

where the aperture constant B was read off from a chart. The deviation of the measurement results from the predicted values is acceptably small, as can be seen in fig 2.5(b).

An improvised resonator. In this last experiment in the S-band a simple waveguide resonator was assembled. This was done by putting a copper foil with a 12mm circular centered hole at the reference plane and terminating the waveguide by a sliding short-circuit. By varying the length of the short the resonator can be tuned. In the

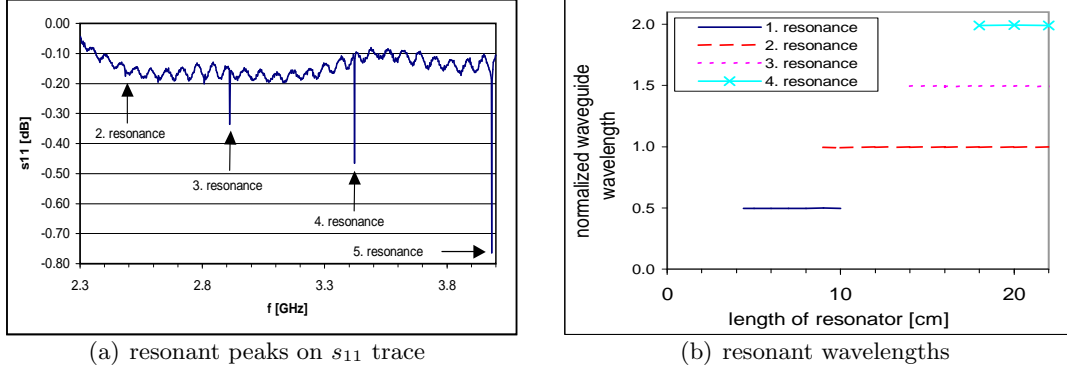


Figure 2.6: An improvised S-band waveguide resonator

reflection's coefficient trace each resonance shows up as a deep valley, see figure 2.6(a). The resonant frequencies were measured and normalized to λ_H . In figure 2.6(b) the resonant wavelengths are plotted over the resonator length. Because the mode coupling is done by the small hole in the conductive foil, this plane acts quite like a short circuit, thus we have got a $\lambda/2$ -resonator. Note also that the strength of the coupling changes with frequency. The determination of the resonant frequencies can be done with very good accuracy, and we will take profit from this fact in the later sections.

2.5 Waveguide calibration for a C-band waveguide

For a second series of tests on waveguides, a C-band rectangular waveguide of proportions $a = 47.55\text{mm}$ and $b = 22.15\text{mm}$ was used. The three calibration standards were equally a matched load and two shorts having the lengths $l_1 = \lambda_0/8$ and $l_2 = 3\lambda_0/8$, respectively. The first cut-off frequency falls to $f_c = c_0/(2a) = 3.152\text{GHz}$, the second to $2f_c = 6.305\text{GHz}$. As done above, we chose the geometrical mean of the limits as center frequency for the definition of the calibration standards, $f = \sqrt{2f_c} = 4.458\text{GHz}$.

Our two shorts then have the lengths $l_1 = 11.9\text{mm}$ and $l_2 = 35.7\text{mm}$, which corresponds to offset delays of $t_1 = 39.65\text{ps}$ and $t_2 = 119.0\text{ps}$. The frequency range for the calibration was set from 3.95 to 5.85GHz to fulfill the specification of the waveguide used. With these parameters the calibration kit was defined. The actual calibration was done with the sliding short and the fixed load.

To test the quality of the calibration, we connected the coax adapter to a 10dB directional coupler (Fairchild 374-10). We found that s_{11} stays well on the outer circle of the Smith chart for purely reactive loads and the initial pulse (the pulse at $t = 0$) does not grow beyond 7mUnits in absolute magnitude, while the reflection of the matched load is about 12mUnits high. However, close to 4.9GHz the calibration seems to fail slightly, as s_{11} falls by 0.7dB for purely reactive loads.

So the calibration had to be redone. Now the results were very satisfying with an initial reflection of $s_{11} = 3.5\text{mUnits}$ and final reflection of some 8mUnits. It seems that we are now close the optimum calibration possible with this equipment, because just under the influence of the drift of the VNA, the initial pulse doubles its amplitude after some minutes without any manipulation.

2.5.1 Calibration in spite of badly estimated cut-off frequencies

A supplementary test that was not envisaged for the S-band waveguide was performed in the C-band: On the Cal-Kit we modified the cut-off frequency of the standards. As it is very hard to calculate where exactly the cut-off of the beam-pipe will be, it may be useful to know how the calibration reacts on errors on the cut-off frequency.

In a first step, f_c was decreased by 2% to 3.089GHz, leaving all other parameters unchanged. In the Smith chart the calibration proves to be very bad, for pure reactances the circle is heavily distorted. In log magnitude representation the maximum error amounts to -1.2dB. It seems astonishingly however that in a large frequency span the calibration is nearly as good as before. In the time domain however the results are not terribly altered, a part from the initial peak that grows.

In a second experiment, the cut-off frequency was augmented by 5% to 3.3096GHz. In the Smith chart the curves do not much resemble any more to the good measurements, while we find large errors of up to 3dB in the log magnitude representation.

Time drift of the calibration. In the C-band we observed a significant drift of the calibration. Various reasons can come into question:

- Internal drift of the VNA
- Changes in the room temperature and heating of the equipment
- Effects of mechanical manipulation on connectors and cables

The first suspicion, that the phenomenon had to do with the VNA's internal drift proved wrong. In uncalibrated mode the VNA's drift of the log magnitude response in the frequency domain is below 0.05dB over short periods. For one hour it increased to only 0.1dB, which is much smaller than the variations observed.

Changes in temperature may play a role, but when the power dissipated in the assembly is low and no external heat sources such as radiators or direct solar irradiation influence the set-up this effect can be neglected.

The last point proved to pose a problem: Mechanical manipulations on the cables and to a certain degree on the connectors changed significantly the frequency response. But those manipulations cannot be avoided. This makes that every time a cable is branched or even moved, its frequency response gets more different from its original one during calibration.

Influence of the cables. The observations described above adverted us that the variations introduced by the cables play an important role in the measurements. This is why we did a little performance test on 4 different cables: the variation of the cable's frequency response was observed when common manipulations such as bending, twisting, fastening or unfastening connectors are done. Just the first cable turned out to be suitable for reliable calibration.

type of cable	max. variation [dB]
60cm copper-shielded polyethylene measurement cable	< 0.05
30cm copper-shielded cable, connectors type "self-made"	< 0.5
155cm copper-shielded RG 142 DU cable	< 0.5
75cm RG 214U	< 2

Automatic power adjustment. We observed that the noise level far from any pulse depends on the amplitude of the strongest reflection.² On the HP8753 we found an increase in dynamic range³ from 84dB to 92dB when the amplitude of the highest pulse was decreased by 20dB in calibrated mode. For uncalibrated measurement the dynamic range seems to be close to 95dB, as before independent of the amplitude of the highest pulse. Apparently some kind of range switching is done before the VNA's ADC in dependence of the incoming power. For measurements on a long line, the effective noise level can therefore be reduced by avoiding large reflections close to the beginning of the line.

2.6 Waveguide calibration on the beam-pipe

For later measurements on the beam-pipe a waveguide calibration would be desirable. But unlike for ordinary waveguides, no standard components are available when working with the beam-pipe. The calibration procedure however should stay the same as before: define a suitable Cal-Kit, take two shorted waveguides and one load, branch them to the coax adapter, let the VNA do the calibration and that's it!

So we had to do a little “bricolage”: The coax adapter was tinkered with a beam-pipe to circular waveguide junction into which we soldered a piece of circular guide (figure C.3(a)). An N-type coax connector was mounted at the end plate, its inner conductor passing through a hole into the circular waveguide. For measurements with the TM mode we usually used an axial pin that was shorter than $\lambda_0/4$, having a length of up to 15mm. As calibration standards we took three short pieces of beam-pipe. The shorts were realized by soldering brass plates at approximately 7.34mm and 20.35mm. These lengths correspond to roughly $\lambda_0/4$ and $3\lambda_0/4$ at $f = 5.5GHz$, they were chosen as high as possible to reduce sensitivity regarding mechanical uncertainties and handling. For these two shorts the calibration becomes singular for $f \approx 9GHz$, which is sufficiently far from our operating range that goes up to 8GHz. The load was simply made by stuffing absorbing material into a short piece of beam-pipe. The calibration standards and the excitation element are shown in the figures C.2(b) and C.4(b). The calibration for the TM mode thus obtained proved quite well taken into account that there are other modes present and that the repeatability of the contacts is difficult to assure. Measurements on longer sections will show if it is advantageous to use waveguide calibration on the beam-pipe.

²This is the case for the first network analyser used, the HP8753 as well as for the Agilent E8358

³Ratio of highest amplitude over RMS noise level in time domain

Chapter 3

Resonator measurements with the beam-pipe

For the performance of the reflectometer it is crucial to know the accurate cut-off frequency and the attenuation of the modes of interest in the beam-pipe. Theoretical calculations indicated roughly in which range to look, but for such a non-standard waveguide profile as the LHC beam-pipe, an exact determination by measurement is indispensable. Furthermore the influence of the slots had to be determined, especially on the TE modes that will disturb us. To obtain accurate data, we decided to build a simple waveguide resonator with two pieces of beam-pipe, a slotted one and an unslotted one for reference measures (profiles in fig. 3.1(b)) of length 1m and 1.2m, respectively. At each end of the pipes we soldered a solid brass plate of 10mm width to get a good short-circuit. In the center of the brass plates we had to drill a small hole of 10mm diameter, on the outer side of which we fixed an N 50Ω connector. The inner conductor can then be passed through the hole to excite the desired waveguide modes. A photo of the two resonators is shown in fig. C.5

3.1 The cut-off frequencies

Experimentally the cut-off frequency can be roughly estimated for good SNR in direct transmission measurement, but there is a better way to find out:

When observing a row of peaks on a resonator, the cut-off frequency can be obtained by reading off the respective frequencies of the peaks. It is given by the formula

$$f_c = \sqrt{f_n^2 - \left(\frac{nc_0}{2l}\right)^2}, \quad (3.1)$$

with f_n standing for the frequency of the n^{th} peak on a resonator of length l , as is derived in A.5. There remains, however, the uncertainty concerning the choice of the first peak, that is, if the first peak measured was really the first resonance. Close to cut-off strange things can happen, for example that a resonance peak is not recognised, especially with other modes present. This is why we have adopted a simple trial and error strategy: the indices n are tried out, and if the resultant cut-off frequency stays fairly constant for all peaks, you've won. This method is demonstrated in table 3.1 with first TM mode of the unslotted beam-pipe.

f_{meas} [GHz]	n	f_c [GHz]	n	f_c [GHz]	n	f_c [GHz]
5.5660	1	5.5646	2	5.5604	3	5.5534
5.5730	2	5.5674	3	5.5604	4	5.5506
5.5790	3	5.5664	4	5.5567	5	5.5440
5.5890	4	5.5667	5	5.5541	6	5.5387
5.6030	5	5.5682	6	5.5528	7	5.5346
5.6170	6	5.5669	7	5.5488	8	5.5277
5.6550	7	5.5872	8	5.5663	9	5.5425
5.6790	8	5.5907	9	5.5670	10	5.5404
5.7050	9	5.5935	10	5.5670	11	5.5376
5.7340	10	5.5967	11	5.5675	12	5.5353
5.7640	11	5.5984	12	5.5664	13	5.5313
5.7980	12	5.6016	13	5.5667	14	5.5289
5.8350	13	5.6053	14	5.5677	15	5.5270
5.8730	14	5.6075	15	5.5671	16	5.5237
5.9130	15	5.6093	16	5.5662	17	5.5199
5.9570	16	5.6129	17	5.5670	18	5.5179

Table 3.1: The trial and error method for the indices of the resonant peaks. Just in the second column the calculated cut-off frequencies do not change much \Rightarrow the indices are well assigned!

If the indices are too small, the values for the calculated f_c will increase, while they decrease if n is chosen too large. For the right choice, the f_c should stay constant within measurement uncertainty. In this case e.g. the standard deviation of f_c amounts to 10.3MHz, which is less than 0.2%.

On the theoretical side, to get a reasonably good idea, we chose two kinds of approximation: a circumscribed rectangular and two circular waveguides, one inscribed and one circumscribed, see table 3.1. The circumscribed rectangular waveguide should provide a lower limit for the cut-off frequencies while the inscribed circular profile should be a higher boundary (fig. 3.1(b)). A comparison of the measured to the calculated values according to [2] is shown in table 3.1.

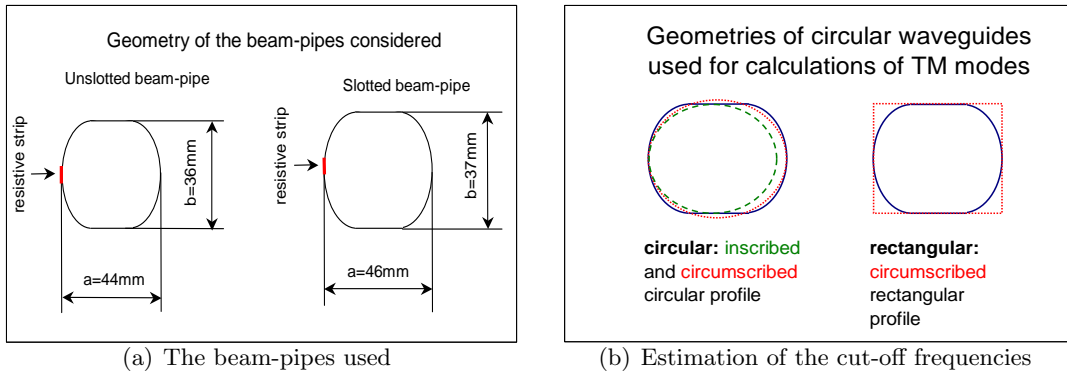


Figure 3.1: The geometries of the beam-pipes used

Waveguide Mode	circular circumscribed	circular inscribed	rectangular circumscribed	measured on beam-pipe
$TE_{\bigcirc 11}, TE_{\square 10}$	3.82	4.75	3.26	3.61 ($TE_{\bigcirc c11}$)
$TE_{\square 01}$	-	-	4.05	4.32 ($TE_{\bigcirc s11}$)
$TE_{\bigcirc 21}, TE_{\square 11}$	6.34	7.88	5.20	-
$TE_{\square 20}$	-	-	6.52	-
$TM_{\bigcirc 01}, TM_{\square 11}$	4.99	6.20	5.20	5.33 ($TM_{\bigcirc 01}$)
$TM_{\bigcirc 11}, TM_{\square 21}$	7.95	9.88	7.67	7.99 ($TM_{\bigcirc 11}$)

Table 3.2: The estimated cut-off frequencies for the slotted beam-pipe compared to the measured values, in GHz.

In order to differentiate between circular, rectangular and beam-pipe shaped waveguides, we always add the symbol \bigcirc for the circular, \square for rectangular and \bigcirc for the beam-pipe shaped waveguide whenever we talk of more than one type of waveguide. For the special case of the beam-pipe, our nomenclature follows the analogy to the elliptic waveguide, so the two polarizations of the $TE_{\bigcirc 11}$ mode on the beam-pipe will be called $TE_{\bigcirc c11}$ ("c" for cosine-polarization, the E-field parallel to smaller side) and the second TE mode $TE_{\bigcirc s11}$ ("s" for sine-polarization, the E-field parallel to longer side), and the same way for all the other modes.

As can be seen in figure 3.1(b), the approximation with a circumscribed circular profile seems to fit best, at least geometrically. For the $TE_{\bigcirc c11}$ and the $TM_{\bigcirc 11}$ modes it fits closest to the experimental data. The rectangular circumscribed waveguide has generally smaller cut-off frequencies due to the significantly larger proportions. It is surprising that the measured $TM_{\bigcirc 01}$ cut-off frequency is even higher than the predicted values for a circular circumscribed waveguide. The second disturbing TM mode appears as predicted, since the beam-pipe being a flattened circle, facilitates the propagation of this mode, as can be seen from the field profile. The two symmetrical parts of the $TM_{\bigcirc 11}$ mode fit better into a flat profile than into a circular one.

With regard to the planned reflectometer it has to be stated that there is a frequency band 2.6GHz wide where the $TM_{\bigcirc 01}$ mode is the only TM mode that can propagate. Since we have to keep a certain distance from our mode's cut-off as well as from the second TM mode, the *operational frequency range* will lie between 6.0 and 7.9GHz.

3.2 The attenuation measurement

In [12] a very precise measurement method for resonators in transmission mode is presented. It is pointed out that the SNR in transmission mode is much superior to the one in reflection mode. For the unloaded Q_0 factor the formula

$$Q_0 = Q_L(1 + \beta_1 + \beta_2) \quad (3.2)$$

is presented. Q_L represents the measured loaded Q factor for the system and the coupling coefficients β_1 and β_2 represent the ratio of the external power dissipated to the power dissipated in the system. If the mentioned coupling coefficients are much smaller than 1, then the external losses can be neglected and $Q_0 \approx Q_L$. For our purposes it was sufficient to monitor the strength of coupling by watching the local drop of s_{11} and s_{22}

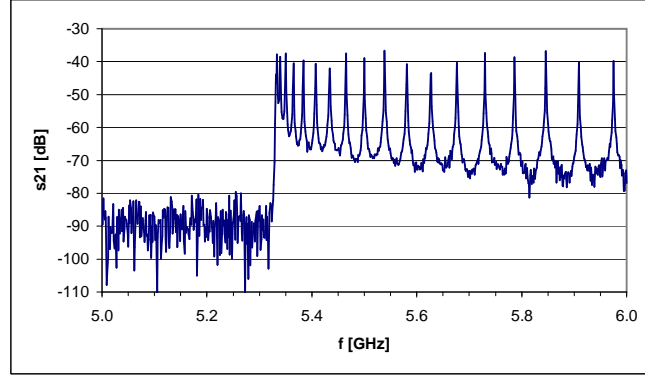


Figure 3.2: The characteristic pattern of resonance peaks for the TM_{001} mode on the slotted beam-pipe

at the resonance frequencies. A more rigorous treatment can be found in [14], including the case of non-negligible drops of s_{11} and s_{22} .

The attenuation was then calculated using the formula

$$Q = \frac{\pi \lambda_H}{\lambda_0^2 \alpha} \quad (3.3)$$

where Q represents the measured loaded quality factor, α is the attenuation in Np/m and λ_H the guided wavelength [11].

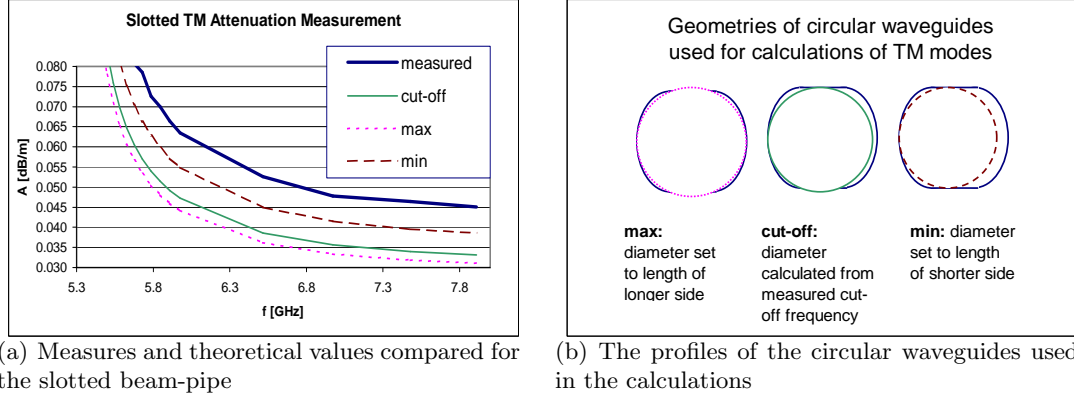
3.2.1 The TM mode

The TM modes were excited simply by the stumps of some 2mm length of the inner conductors of the N type connectors reaching into the drilled hole in the center of the brass plate. The end of these stumps is still some 6mm inside the hole, as seen from the waveguide (see fig. C.4(a)). This way, the coupling is very weak and the resonator achieves high quality. Because of the circular symmetry of the exciting element, the coupling is very weak for TE modes, as they need radial currents. Since the cut-off frequency of the the TM_{001} is assumed to be close to 5.5GHz, we made a full two-port calibration between 5 to 6GHz. The s_{11} trace shows little valleys at the resonant frequencies while s_{21} has very distinct peaks (fig. 3.2). The cut-off frequency $f_{TM_{001}}$ falls to 5.33GHz.

Attenuation of the TM_{010} mode. The width of the peaks was measured without calibration. Bearing in mind that the bandwidth is in the order of 300kHz, this does not change significantly the measured Q factor, as the relative amplitude uncertainty of the VNA was found to be within 0.05dB for such a small range and we did not need to measure accurate absolute values.

The quality factor was measured for each good resonance peak from the cut-off up to 8GHz, where the second TM mode comes in. The resulting attenuation was plotted in fig. 3.3(a). For comparison, the curves obtained by evaluation of the formula for a circular waveguide from [1], adapted to copper waveguides and SI unities, are shown.

$$\alpha = 1.19 * 10^{-6} \frac{1}{D/cm} \frac{\sqrt{f/Hz}}{\sqrt{1 - (\frac{f_c}{f})^2}} \quad [\text{dB/m}] \quad (3.4)$$

Figure 3.3: Attenuation of the TM_{O11} mode

It can be seen that the beam-pipe behaves in accordance with the way an almost circular waveguide should do, apart from the fact that the attenuation is between 30 and 50 % higher than for an ordinary circular waveguide, depending on the approximation considered. There is no significant difference between the three approximations, the curves are slightly shifted towards higher attenuation and higher frequencies for smaller circular waveguides. From the theoretical point of view the “most correct” approximation should be the one obtained by using a circular waveguide possessing the same cut-off frequency as the beam-pipe. This is due to the fact that the cut-off determines the location of the “singularity” of the attenuation.

To exclude the influence of bad adaptation, we added, at both ends of the waveguide, attenuators of 10 and 6dB. The quality factor was checked for 3 peaks, and apart from quite poor SNR we discovered significant changes, the quality factors increased slightly by up to 4%. This could be due to the automated measurement method: The VNA tracks the maximum values of the peak and calculates the 3dB bandwidth. In the presence of noise the detected maximum value is higher than normal while the shoulders of the resonance peaks do not change much, so the calculated Q factor becomes too large.

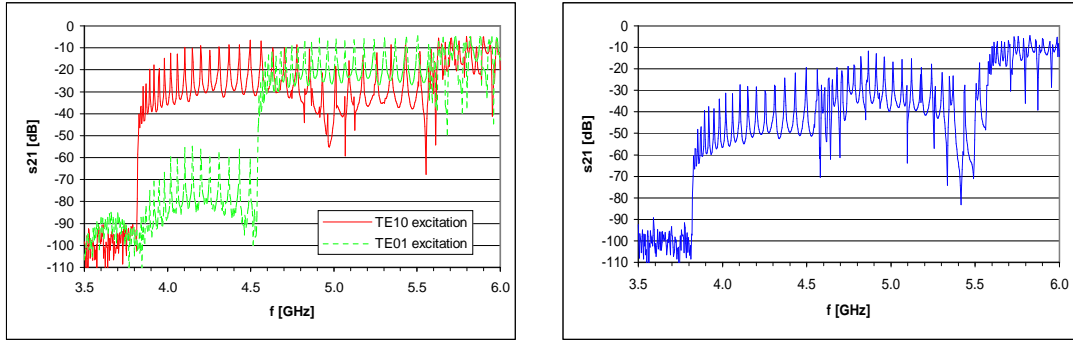
Summing up this little check, we can say that there are no significant errors present due to coupling. If the results were influenced by external losses, the quality factor should have changed dramatically.

3.2.2 The TE modes

TE modes can be excited by allowing a radial current in the mode launcher. Therefore, we placed a kind of dipole in the center of our waveguide. In order to obtain a weak coupling, some different wire shapes were tested. Finally we just extended the inner conductor with some 6mm of wire in the shape of an improvised dipole. In fact it looked more like a crook or question sign standing on the short-cut plane of the resonator. The part of the wire that carries the radial currents is just some 4mm long and does not reach into the beam-pipe. It was placed towards at the end of the hole in the brass plate in the plane of the short-circuit. This way the coupling effects were sufficiently small to be negligible. There was one case only where the measurement results had to be discarded due to overcoupling. The effect was recognised directly by checking

f [GHz]	Q_L	Δs_{11}	Δs_{22}	A [dB/m]
5.1233	16000	0.12	0.34	0.0570
5.2433	16250	-	0.32	0.0561
5.3066	16000	0.25	0.70	0.0558
5.3721	16400	0.40	0.36	0.0535
5.4397	16200	0.50	0.35	0.0533
5.5091	14450	0.60	2.70	0.0590

Table 3.3: Measurement series for the $TE_{\text{Os}11}$ mode. The effect of overcoupling on the measured attenuation can be seen for the last row, where the attenuation seems to rise, contrary to its natural behaviour



(a) Excitation for the $TE_{\text{Oc}11}$ and the $TE_{\text{Os}11}$ mode (denoted TE_{10} and TE_{01} , respectively)

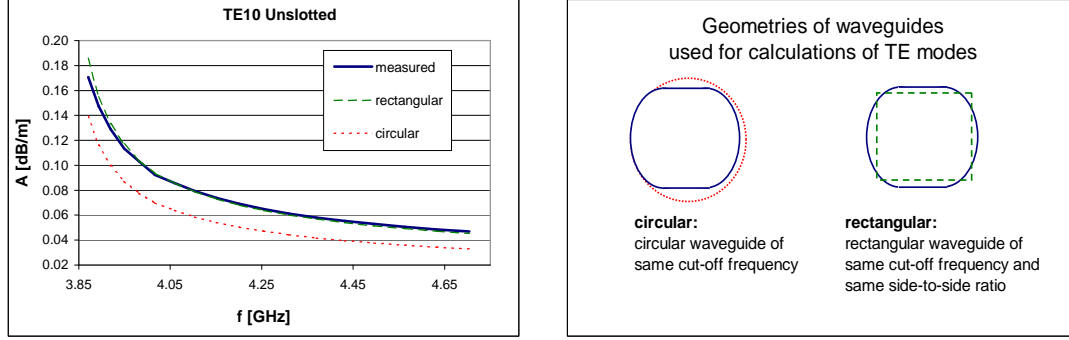
(b) Cross-polarization: the excitation dipoles are oriented orthogonally

Figure 3.4: The unslotted beam-pipe in transmission mode

the drops of the reflection coefficients Δs_{11} and Δs_{22} (see table 3.3). It results in an apparent drop of the measured quality factor and thus in higher attenuation.

We found two distinct TE polarizations similar to elliptical waveguides. The TM cut-off can be clearly distinguished above 5.56GHz, where the trace gets quite mixed up. The first TE mode $TE_{\text{Oc}11}$ starts at 3.61GHz, the $TE_{\text{Os}11}$ joins at 4.32GHz (see table 3.1). For exact measurements of the two TE modes, they have to be excited specifically by orienting the excitation wire in parallel \vec{E} -field of the desired mode. The first mode can also be measured without any precautions, if just the lower frequency band is scanned, where it is the only mode able to propagate.

The $TE_{\text{Oc}11}$ mode was therefore excited by orienting the “dipoles” in parallel to the shorter side of the guide. For direct comparison of the two TE modes the mode launchers were then set to cross-polarization mode by orienting the dipoles orthogonally. Finally $TE_{\text{Os}11}$ excitation was tested. In fig. 3.4 the three measurements performed for the unslotted beam-pipe are plotted. Comparing the $TE_{\text{Oc}11}$ and $TE_{\text{Os}11}$ excitations in the left plot, we can see in the region between 3.9 to 4.5GHz that the cross-polarization attenuation for the $TE_{\text{Oc}11}$ mode amounts to around 50dB. This indicates that the measurements on the $TE_{\text{Os}11}$ mode will not be affected by the presence of the other TE mode. The trace of $TE_{\text{Oc}11}$ however is quite deformed in the region above 4.5GHz where the $TE_{\text{Os}11}$ mode is also present.



(a) Measured attenuation compared to theoretical values for two approximations for the fundamental TE mode

(b) The geometries used for the calculation of the TE modes on the beam-pipe

Figure 3.5: Attenuation of the TE_{Oc11} mode on the unslotted beam-pipe

Attenuation of the TE_{Os11} mode. For all TE modes there exist azimuthal components of the wall currents. This led us to assume that they would be heavily attenuated by the axial slots on the beam-pipe. In the unslotted beam-pipe the resistive axial strip should also play an important role.

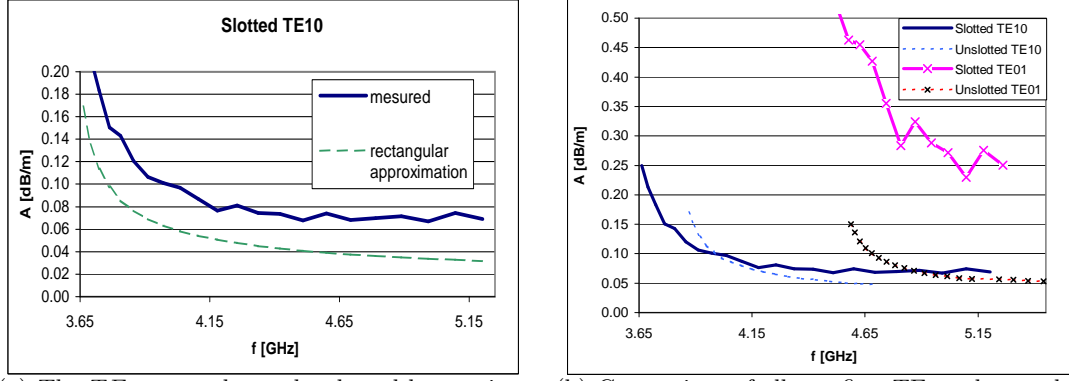
The theoretical values for a rectangular waveguide with sides a and b in [cm] were again found in [1]:

$$\alpha = 1.19 * 10^{-6} \frac{1}{b/cm} \frac{\frac{1}{2} + \frac{b}{a} \left(\frac{f_c}{f}\right)^2}{\sqrt{1 - \left(\frac{f_c}{f}\right)^2}} \sqrt{f/Hz} \quad [\text{dB/m}] \quad (3.5)$$

For the unslotted waveguide we found an attenuation around 50% higher than the predicted values for a similar circular waveguide as illustrated in fig. 3.5(a). The second approximation, a rectangular waveguide comes quite close to the observed behaviour. The diameter of the circular waveguide and the length of the longer side of the rectangular waveguide were calculated under the condition that the cut-off frequency be the same as for the beam-pipe (fig. 3.5(b)). As the geometry of the rectangular waveguide is determined by two parameters, the ratio of the two sides of the waveguide was set to the beam-pipe's. The relative large deviation for the circular approximation can be explained by the fact that TE modes do not have axial symmetry, they do not "fit" well into circular profiles and therefore have higher cut-off. If the cut-off frequency is held constant, the proportions of a circular waveguide will be larger and attenuation underestimated. Likewise the attenuation of the rectangular waveguide approximation is relatively large, the proportions of the rectangular profile being relatively small.

On the slotted beam-pipe we expected to find a much larger attenuation. However, at least for the TE_{Oc11} mode, this is not the case. Fig. 3.6(a) shows that in the slotted beam-pipe the TE_{Oc11} mode is attenuated only twice as much as in the unslotted one. Since the rectangular approximation came so close for the unslotted case, we can say that in spite of the little change in geometry - the slotted beam-pipe is slightly larger the unslotted one - the approximation predicts well the behaviour of the beam-pipe without slots.

Note that the measured curve flattens for $f > 4.4\text{GHz}$. This is not typical so close to cut-off!). In this region the radiation losses from the slots begin to prevail over the



(a) The TE_{Oc11} mode on the slotted beam-pipe compared to the theoretical curve. The theoretical curve should come quite close to a beam-pipe without slots.

(b) Comparison of all two first TE modes on the slotted and the unslotted beam-pipe. Note that the slotted pipe is larger \Rightarrow higher cut-off and attenuation

Figure 3.6: Attenuation of the TE modes on the beam-pipe

resistive losses. For the area of operation of the reflectometer ($f > 6\text{GHz}$), we can be confident that the TE_{Oc11} mode will be attenuated by 0.07dB/m at least.

Attenuation of the TE_{01} mode. The TE_{Os11} mode reacted according to expectations: Here the slots provide for an increase of attenuation by a factor 5. It is clear that this mode suffers most, because it has its maximum wall currents on the longer side of the waveguide, just where the slots are situated. On the other hand it should be almost completely insensitive to the welding, as this resistive strip falls to a zero point of the azimuthal wall currents.

All the TE measurement data are combined in the fig. 3.6(b).

3.3 Check on a rectangular C-band waveguide

The results we presented in the previous parts of this section are essential for the good function of the reflectometer. To be sure that they can be relied on we performed a cross-check of our measurement technique with an ordinary rectangular C-band copper waveguide of dimension 47.55x22.15mm. On this waveguide, only the $TE_{\square 10}$ mode was in the range of the VNA used, the HP 8573D, all other modes having cut-off beyond 6GHz. This test allows us to exclude error sources such as mode mixing, the non-standard waveguide profile, slots and resistive strips as they are encountered when working with the beam-pipe. For rectangular waveguides there is no need to do any approximation, the theoretical formulas should be valid without constraint. The only cause of significant deviations, a part from the measurement set-up, can be the roughness of the waveguide surface and eventually some dust that has settled down.

Clearly, there should be nothing easier than doing these few standard measurements on an ordinary waveguide. However, this was absolutely not the case.

We tried to construct good resonators with two different waveguides of length 39 and 100cm, respectively. Since the waveguides had been out of use, stacked in some dark storehouse for some years, we passed the shorter one first through mechanical and then through dry-cleaning. The ends of the waveguides were short circuited by

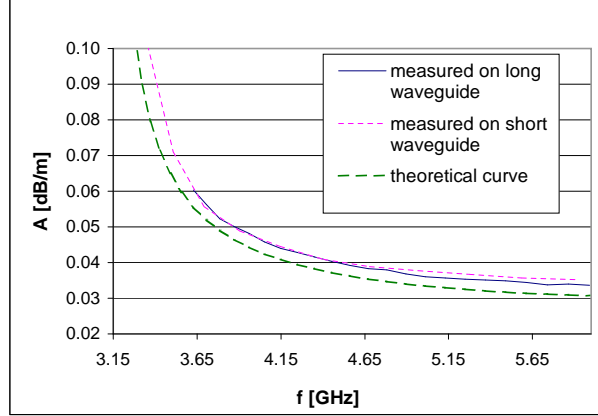


Figure 3.7: Check of the reliability of resonator measurements: attenuation for a standard rectangular C-band waveguide resonator compared to the theoretical values. Length of the short and long resonator: 39cm and 100cm, respectively

two solid brass-plates, with s_{11} very close to -1, we were convinced. As before, in the center of the brass plates was a drilled hole, through which the inner contact of the N-connector was passed. According to various parameters such as the waveguide used, the strength of mechanical contacts, etc. we got unexpected results. The attenuation measured exceeded the predicted values by up to a factor 5. What was wrong?

Well, the solution to the problem were the contacts between the more or less plane brass plates and the flanges of the waveguide. This contact not being well defined for high frequencies, the quality of the resonator can become quite bad.

To avoid this problem we improved the contacts by inserting a small copper foil between the flanges of a normal TE_{10} waveguide adapter and the straight waveguide. The foil was well centered and its proportions were chosen to be just little bit larger than the waveguide aperture, by around 1.5mm on each side. A picture of this construction can be found in figure C.6(a). Fixing mechanically the adaptor onto the waveguide provided then for good contact at the ends of the resonator, close to the walls of the waveguide. The coupling was provided for by two small triangular holes with a surface of some $5mm^2$ in the center of the foils. The coupling was observed to be very small, s_{11} or s_{22} seldom dropped by more than 0.01dB.

In fig. 5 the results with the conductive foil are shown. For the longer guide the standard deviation of both the obtained f_c and the ratio $\frac{\text{measured attenuation}}{\text{theoretical attenuation}}$ are smaller than for the short waveguide. This could be due to the fact that for a longer resonator the influence of perturbations from the end planes is less important. The attenuation was found to be $8.5 \pm 0.8\%$ higher than the theoretical values for the long waveguide and $10 \pm 3\%$ for the short one.¹

The measurement of the cut-off frequencies also proved quite accurate. We found that the mean of the calculated f_c was much closer to the theoretical value than the standard deviation of the measured series. This indicates that the assumption of a Gaussian distribution is too pessimistic. However, even from the pessimistic point of view the deviation from the theoretical values was less than 1‰ for the long and 3‰ for the short resonator.

¹The given uncertainties correspond to $\pm 1\sigma$, assuming Gaussian error distribution

3.4 Attenuation at 20K

At low temperature the attenuation is expected to decrease considerably. This would allow us to extend the range and the sensitivity of the reflectometer. It is not so easy however to give good numbers since the attenuation is not solely dependent upon the resistance of the copper. Leaving the interconnects for the next section, we still have to deal with at least 5 significant components:

1. The RF resistance of the copper cladding. Since the thickness of this layer is much larger than the skin depth δ in our frequency range ($\delta < 3\mu m$ for $f > 5GHz$), the standard formula for waveguide attenuation can be used.
2. The additional resistance due to the longitudinal welding strip (resistive strip in fig. 3.1(a))
3. The corrugations in front of the welding strip that are meant for capturing the synchrotron radiation.
4. The radiation through the slots.
5. The general surface roughness

The wall resistance. The first effect is present for every waveguide and has been treated adequately in the beginning of this chapter. For the TM_{001} mode the measured attenuation lies between 30 and 40% above the values calculated for similar geometries, the deviation growing slightly with frequency. This tendency provides for a possible source of the additional attenuation, as not all the four effects have the same dependence on frequency. The standard resistive attenuation for the TM_{001} mode goes with $\frac{\sqrt{f}}{\sqrt{1-(\frac{f_c}{f})^2}}$ and can be very well approximated by using the standard formula for a circular waveguide with the same cut-off as the beam-pipe (3.4).²

The RRR³ of the copper cladding of the beam-pipe is difficult to evaluate. In a diffusion process, impurities from the stainless steel drift into the copper layer. The concentration of those impurities decreases when going from the steel towards the center, but close at the interface copper-air the atoms are stopped and accumulate. Therefore the conductivity at low temperature reduces significantly when approaching the surface of the cladding. At room temperature the depth of penetration is in the order of $0.1\mu m$ in our range of operation. At low temperature it reduces, which suggests that the deterioration of the RRR close to the surface has even a higher impact. The calculations of the RRR vary much in the region of 0.01 to $0.1\mu m$, so we can only roughly estimate that $RRR \approx 20$. For operation under high magnetic field, the magneto-resistive effect may cause the resistivity to increase by a factor 2 as a first approximation. Assuming $RRR = 20$ for the following calculations, we get a decrease in surface resistance and attenuation by a factor $\sqrt{20} = 4.5$.

The welding strip. The influence of the welding strip has already been subject to extensive research. It was found out that the wall current distribution of electromagnetic

²This was actually the reason for choosing the waveguide having the same cut-off as most appropriate approximation

³Residual resistivity ratio, ratio of the resistivity at room temperature to the normal conducting resistivity at a given low temperature, in our case 20K, which depends heavily on the materials purity

waves does not change significantly in the presence of the strip. This allows a simple scaling with the resistance of steel over 2mm of circumference and copper on the other 140mm. The specific resistance of stainless steel being roughly 23 times larger than that of copper [13], it will present $\sqrt{23} = 4.8$ times more resistance to the electromagnetic waves. The resistance scales only with \sqrt{f} because skin depth decreases with \sqrt{f} . Thus, 2mm of stainless steel will be responsible for a relative attenuation of $4.8 \frac{2\text{mm}}{140\text{mm}}$, an increase of almost 6%. At low temperature the conductivity of copper decreases, while the welding conductivity is hardly affected [13]. Therefore this effect will become about four times more important at 20K, being responsible for about 20% of the losses during operation.

The corrugated surface. The surface roughness will have an effect similar to that known from strip lines. In [14] the surface resistance of a tube with entirely ribbed surface was measured with the coaxial wire method up to 2GHz. At room temperature, the change of surface resistance seems to go almost linearly with frequency, reaching 10% at 2GHz. Scaling to the beam-pipe, where the corrugation covers just 15mm of the circumference, and for a frequency of 6GHz, it results in an increase of the surface resistance of $10\% \frac{15\text{mm}}{140\text{mm}} \frac{6\text{GHz}}{2\text{GHz}} \approx 3\%$ at room temperature. At 2K however, the surface resistance of corrugated tube is the same as for a smooth one, which is quite remarkable [14]. Extrapolating from these data to the operation temperature of around 20K, the increase in attenuation is an order of magnitude lower than at room temperature and can therefore be neglected.

The slots. The evaluation of the radiation losses through the slots would require extensive theoretical calculations in order to find a proper solution. The coupling through the slots to the coaxial waveguide, consisting of the beam-screen and the surrounding cold bore, was already treated in several publications [13]. To minimize coherent coupling the lengths of the slots were varied. However, most of these tests were performed for frequencies out of our range of operation. So, to get a rough idea we did a simple experiment:

We took the slotted resonator described in the beginning of this chapter and with conductive glue we bonded a copper foil onto the slots. The Q factor even diminished a little which seems to be due to the fact that the glue is not such a good conductor at very high frequencies. Since the slots can be treated as small cut-off channels, it is safe to assume that there will be just a small impact on the field distribution *in* the beam-pipe. This was confirmed by the fact that the Q factor does not change much. Instead of radiating to free space, the wall currents pass through the resistive glue and the copper foil (fig. C.6(b)). As we wanted just a reliable upper limit for the radiation passing through the slots, we uncovered two adjacent perforations at a total length of 1.5cm, corresponding to 0.38% of the slots of this sample of beam-pipe. This length is much smaller than the guided wavelength, therefore not much destructive interference can occur when measuring near the resonator. A “far-field” measurement of the radiation pattern of the resonator proved too complicated with all those side lobes around. We measured at the frequencies of the resonance peaks

- the local drop of s_{11} that corresponds to the power going into the resonator, referred to as s_{11})⁴

⁴For the ease of explanation we will always use the slightly misleading expression “power” when

Mode	$TM_{\text{O}01}$	$TM_{\text{O}11}$	$TE_{\text{c}11}$	$TE_{\text{s}11}$
s_{Rtot} [dB]	-21	-15	-8.4	-3.3

 Table 3.4: The measured power radiated through the slots, s_{Rtot}

- the power radiated through the two uncovered slots s_R .

The second variable was measured by shifting the position of a C-band waveguide to coax adaptor to find maximum transmission. The end of the resonator was not equipped with an exciting element but just with a solid short. Now a simple energy balance can be drawn:

The power going into the resonator, s_{11} , has to be equal to the power dissipated plus the power going through all the slots, s_{Rtot} . Assuming as a worst case that for more slots the resonator will radiate coherently, the total radiated power s_{Rtot} is found by multiplying s_R with the total number of slots over 2. The ratio $\frac{s_{Rtot}}{\sqrt{1-s_{11}^2}}$ finally gives the fraction of power going through the slots. The values obtained vary over quite a large range, due to the quite primitive measurement procedure and the fact that the radiated power goes with the square of the wall current at the position of the perforations. Therefore the amplitude of s_R is dependent on the standing wave pattern. When a maximum coincides with the position of the slots, the calculated s_{Rtot} will be overestimated by 3dB since the maximum of a sine wave is twice its RMS. Otherwise, s_{Rtot} can become arbitrarily small in principle. So the minimum values measured for s_{Rtot} minus 3dB gives roughly the power radiated through the slots. The values for s_{Rtot} were corrected for this effect as well as for line attenuation. The two terms almost cancelled each other out. The remaining uncertainties are the estimation of the total radiated power and the search for the transmission maximum with the waveguide adapter.

The minimum values for the most important modes are shown in table 7. For the $TM_{\text{O}01}$ mode, the fraction of power radiated away should be 20dB below the cumulative losses of all the other effects at room temperature. Therefore, it can almost be neglected even for the low temperature case. As expected the TE modes suffer much more from radiation, especially the $TE_{\text{s}11}$ mode, as observed earlier in this chapter. This mode helps to validate the significance of the measurement performed. Fig. 3.6(b) shows the TE modes' attenuation obtained by the much more reliable direct measurement on the resonator. For the $TE_{\text{s}11}$ mode, the attenuation increases by a factor 5 due to radiation losses, so almost all of the power radiates away, corresponding to an s_{Rtot} close to 0dB. The -3dB obtained previously appears to be a good approximation despite the simplifications and the custom-made assembly that we used. Thus we can say that the power lost by radiation for the $TM_{\text{O}01}$ mode is *at least* 16dB below the other losses at room temperature, corresponding to 2.5%, with 2dB of margin included.

The different effects leading to attenuation are summarized in table 7 for the $TM_{\text{O}01}$ mode. The values for the wall resistance listed are not theoretical but extrapolated from measured curves. They possibly contain the cumulated effects of measurement errors, general surface roughness, losses in the brass plates, in the soldering joints and others.

talking about S-parameters that of course have the unit $[\sqrt{W}]$. All numerical values will be given in dB or in power ratios.

Effect	wall resistance	welding	corrugations	slots	total
dependence on f	$\propto \frac{\sqrt{f}}{\sqrt{1-(\frac{f_c}{f})^2}}$	small	small	$\propto f^2$	
dependence on T	decreases with T	const.	roughly $\propto T$	const.	
attenuation @300K	0.045dB/m	6%	3%	< 2.5%	0.05dB/m
attenuation @20K	0.010dB/m	20%	$\ll 1\%$	< 10%	0.014dB/m

Table 3.5: The attenuation for the fundamental TM mode on the beam-pipe. The numerical values in the three columns, welding, corrugations and slots are relative to the wall resistance in the second column. The total attenuation @300K (in bold letters) is the only measured value; all the others are based on estimations

The estimation for the attenuation at low temperature could still be compromised, if the influence of general surface roughness, which is hard to evaluate, plays a crucial role.

For the TE modes the situation is different: The TE_{c11} mode has almost the same total attenuation at room temperature as the TM mode ($\approx 0.05\text{dB/m}$). It can be assumed that the measurement introduces roughly the same error for the first and the second TE mode. For the latter we can be sure that s_{Rtot} was overestimated by some 3dB. Supposing that this happens also for the TE_{c11} mode, we get radiation losses of -5dB or 30%. At low temperature radiation becomes more and more important, constituting at least 70%. Considering the other effects (welding and corrugations), there should not be a significant difference in behaviour than for the TM mode.

Interpolation of the losses due to radiation from direct resonator measurements. Another property of the radiation allows us to crosscheck the more or less reliable results obtained above: Its frequency dependence. As a first approximation we can assume that the radiated power goes with the frequency squared. Therefore we can decompose the attenuation measured in the beginning of this chapter in two components:

$$\alpha_{meas} = c\alpha_{theo} + \alpha_{rad} \quad [\text{dB/m}] \quad (3.6)$$

where α_{meas} , α_{theo} , α_{rad} and c represent respectively the measured attenuation, calculated attenuation for a similar waveguide profile, the attenuation due to radiation and a scaling coefficient. Dividing by α_{theo} and introducing the frequency dependence of $\alpha_{rad} \propto f^2$ leads to

$$\frac{\alpha_{meas}}{\alpha_{theo}} = c + df^2 \quad [1] \quad (3.7)$$

with the second coefficient d where c and d can be easily fitted to the data vector $\frac{\alpha_{meas}}{\alpha_{theo}}$ at the frequencies f .

Evaluated for the TM_{001} mode this method gave $\alpha_{rad} = 0.004$ to 0.005dB , some 10% at room temperature, a huge discrepancy compared to the results from the radiation measurement. This 10% discrepancy, however, is negligible since even higher values are found for the unslotted beam-pipe. Thus, it has to be due to other effects that have perhaps similar frequency dependence but not necessarily the same temperature-related properties as radiation.

For the TE_{c11} mode we could apply the method, because as mentioned above this mode can be predictably modelled for the unslotted beam-pipe (see fig. 3.5(a)), whereas its properties change dramatically for the slotted version (fig. 3.6(a)). Indeed in this case α_{rad} comes close to 0.04dB/m, corresponding to more 50% of the total measured attenuation between 4 and 6GHz. The discrepancy to the direct measurement is below 6dB, compared to nearly 3dB for the TE_{s11} mode.

Chapter 4

The interconnects

The main components of the LHC are the nearly 15m long twin-aperture high field superconducting cryomagnets. After installation and alignment, the cryomagnets will have to be interconnected. Besides ensuring the continuity of vacuum enclosures, cryogenic circuits, etc. the beam-pipe image currents have to be cared for. The RF bridges designed for this purpose have a very small resistance at low frequency in the range of a few hundred μV . Figure 4.1 shows two representations of the interconnect. For a photograph of an interconnect installed in the test track see fig. C.7(a). Each interconnect has 30 gold-coated contact fingers. Due to vacuum requirements the contact force has to be relatively low to prevent grating when the position of the interconnect is changed. At the outside a flexible RF bellow is situated as extension of the cold bore. When the cryomagnets go through cool-down from 300K to 20K, they contract and the interconnects have to get 52mm longer, the specified maximum contraction is 62mm. During assembly, at room temperature, the contact fingers hardly touch the beam-pipe and the RF resistance can be high, varying much from one interconnect to the next as the RF contacts are not well defined. After cool-down, in operating position the contact fingers are pushed onto the end of the beam-screen, as is depicted in fig. 4.1(b). The properties of the interconnects are crucial for the performance of the reflectometer for various reasons:

- High reflections mean high energy loss for the propagating wave and therefore low range
- Too high reflections from all interconnects make it difficult to see the reflection from one particular interconnect
- Mode mixing will occur predominantly at the interconnects
- Small reflections close to the interconnects could be difficult to distinguish

For all those reasons the interconnects have to be examined thoroughly. The principal parameter to be determined is the reflection coefficient s_{11} for one interconnect. It will depend on the waveguide mode, the frequency and the position of the interconnect, the latter characterised by the length of the gap in the beam-pipe as given in fig. 4.1(b).

At first it was tried to do measurements on an interconnect with some millimeters of beam-pipe soldered onto each end. This assembly proved to be insufficient for the resonator measurement due to the small number of resonance peaks as well as for the

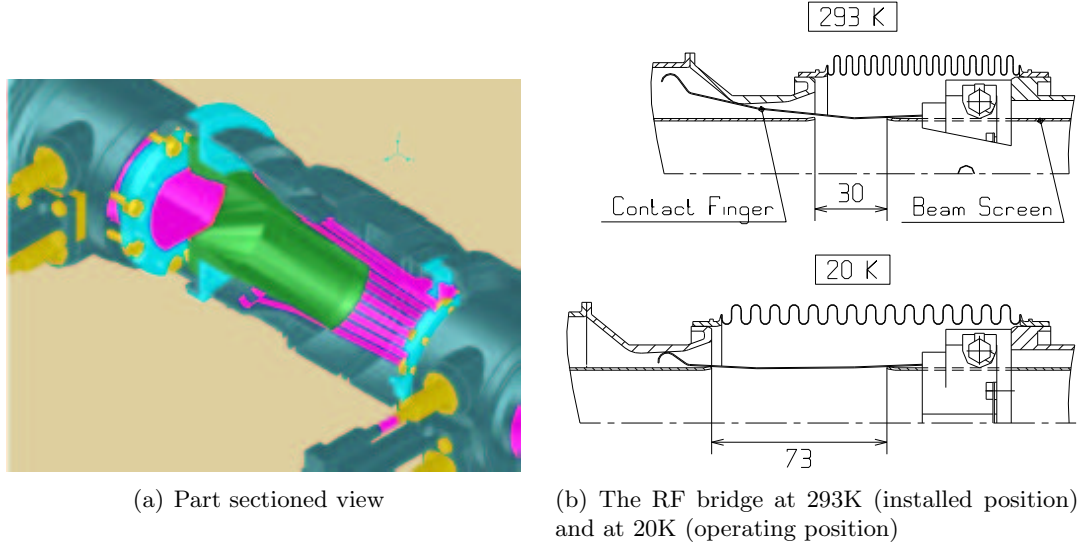


Figure 4.1: The beam vacuum interconnect

reflection measurements, where the spatial resolution was too bad. The measurements were thus repeated for a modified assembly with an additional 75cm of beam-pipe on either side.

4.1 Resonator measurements

The idea of these measurements was to evaluate the “losses” of a TM wave by using the resonator method as before. We expected to find a pattern of resonance peaks, to be able to determine the quality factor and to derive the attenuation per meter as done on the beam-pipe without an interconnect. From the measured overall attenuation we wanted to isolate the attenuation due to the interconnect by subtracting the attenuation of the given length of beam-pipe. The method worked so far, but the curves obtained this way looked *really* strange (fig. 4.2(a)). This is due to the fact that this kind of Q factor measurement makes sense either for a line resonator *or* for a resonator built with discrete elements. The mixture we have before us – 1m of line, the interconnect and another 1m of line – is not so easy to cope with. But perhaps there is still some useful information that can be extracted from this experiment...

So what happens if such a massive perturbation is inserted into a line resonator? In the fig. 4.2(b) the well-known resonance patterns for the electric field of our $\frac{\lambda}{2}$ resonator are plotted. The losses depend essentially on the wall currents that are induced by the magnetic field. For the first resonances the wavelength in the guide is large in comparison to the length of the gap. Considering e.g. the first resonance, it has got a maximum of the E field in the center of the line. Therefore at the location of the interconnect the H field has a minimum, which leads to the supposition that it will suffer only small losses. This is exactly what was found in the measurements. The next resonance on the other hand has a maximum of its H field at the location of the interconnect. Therefore it gets much more attenuated. More generally, odd resonances suffer little attenuation and even resonances much. This leads to the zigzag pattern at

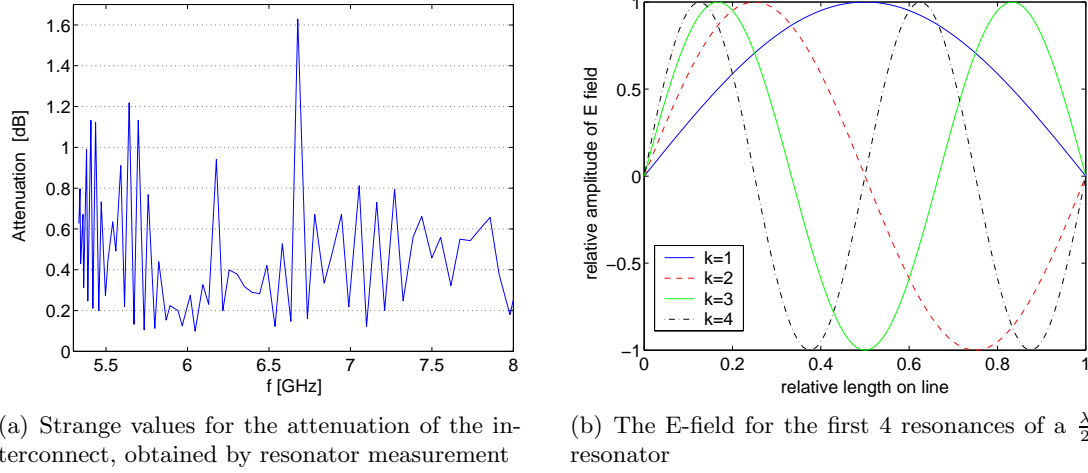


Figure 4.2: The “measurement” of the interconnect’s attenuation using the resonator method

frequencies close to cut-off.

When the frequency gets higher, the guided wavelength gets closer to the dimensions of the interconnect and the above reasoning is no longer valid. More complicated effects determine the shape of the curve in this region.

How should one interpret this weird pattern of peaks and valleys? Neither the attenuation values at the maxima nor in the minima make sense, as they are taken at the maxima and minima of the standing wave. The true values must lie between the two extremes. Therefore we can just assume that they can be found somewhere between 0.1 and 1 dB per interconnect. These losses seem paradox as the interconnect is made of highly conductive copper. The interconnect is a large reactive impedance, indeed, and it causes quite large reflections. However, reflections do not directly lead to dissipation, at least if there is no mode mixing involved, they only detune the waveguide. This should not influence the measurement of the Q factor, apart from the fact that the resonance peaks are shifted in frequency. But there are still several other effects that seem to be the cause of these resistive properties:

- The RF contact resistance of the sliding contact
- The bellow around the interconnect is made of stainless steel, which has considerably higher resistance than copper. Leakage fields, in particular from TE modes that are badly guided by the contact fingers will be much more attenuated
- The two seals where the beam-pipes were welded provisionally
- Other modes that are excited dissipate more energy than the TM mode

4.2 Measurements in reflection mode

For the determination of s_{11} we considered two methods:

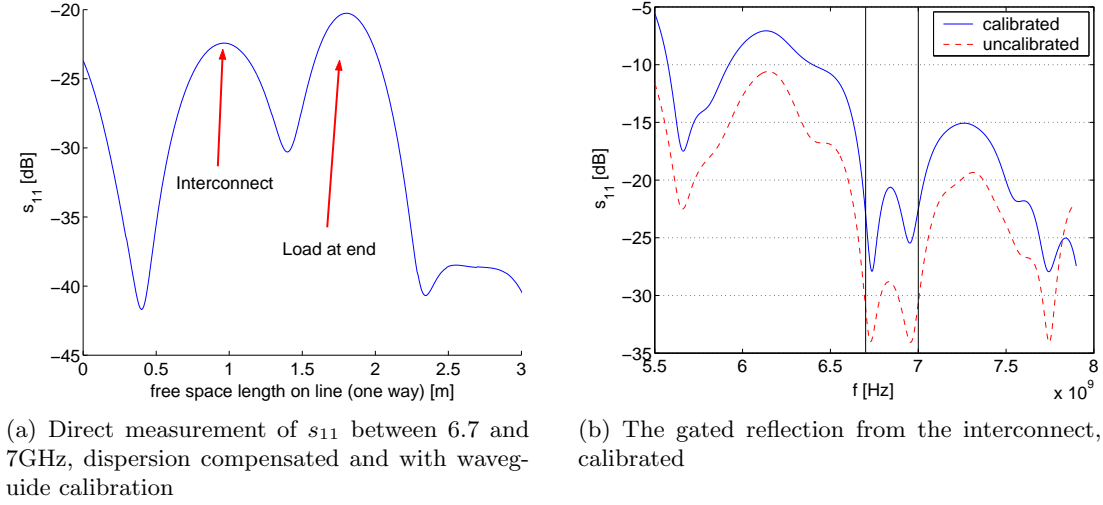


Figure 4.3: Reflection from the interconnect for a length of 63mm

1. **Direct measurement** of s_{11} in a certain frequency range and observation of the peak from the interconnect in time domain
2. **Time domain gating:** measurement of s_{11} over a large frequency span, isolation in time domain of the peak coming from the interconnect by gating and transformation back to the frequency domain

The first method has the advantage of being very straightforward, but it also has some drawbacks: dispersion flattens the peak and power masking becomes important if the first peaks are too high. Moreover it is difficult to observe the frequency dependence of s_{11} .

The second method on the other hand may be less comfortable to apply, but it is not vulnerable to dispersion. Additionally it allows one to find frequency ranges where s_{11} is low, thus making it possible to check results with the first method. Both methods were tried out with and without waveguide calibration.

Figure 4.3 shows the reflection for a gap length of 63mm, which is 1cm smaller than the nominal length at low temperature. The direct measurement of s_{11} was conducted in the frequency range from 6.7 to 7GHz, where the reflection from the interconnect appeared to be lowest. The height of the dispersion compensated reflection of roughly -23dB on the left matches the mean of the gated s_{11} (solid blue line) in the corresponding frequency range in the right plot. Furthermore, comparing the values for the gated s_{11} measured with and without calibration a very good agreement is found. The calibration creates almost no changes to the shape of the curve, but just shifts it upward by 5dB. This attenuation comes from the coaxial cable and the coupling losses from the coax to beam-pipe adapter. For the calibrated measurement the effect of attenuation in the waveguide should be negligible, as it amounts to less than 0.2dB for the path from the coax adapter to the interconnect and back.

The effects of gating were examined by repeating the measurement using a larger frequency span. As expected, just minor changes at the edges of the frequency band were observed. To check the repeatability of the entire measurement procedure, including the mechanical handling (varying the interconnect's length and reconnecting the coax

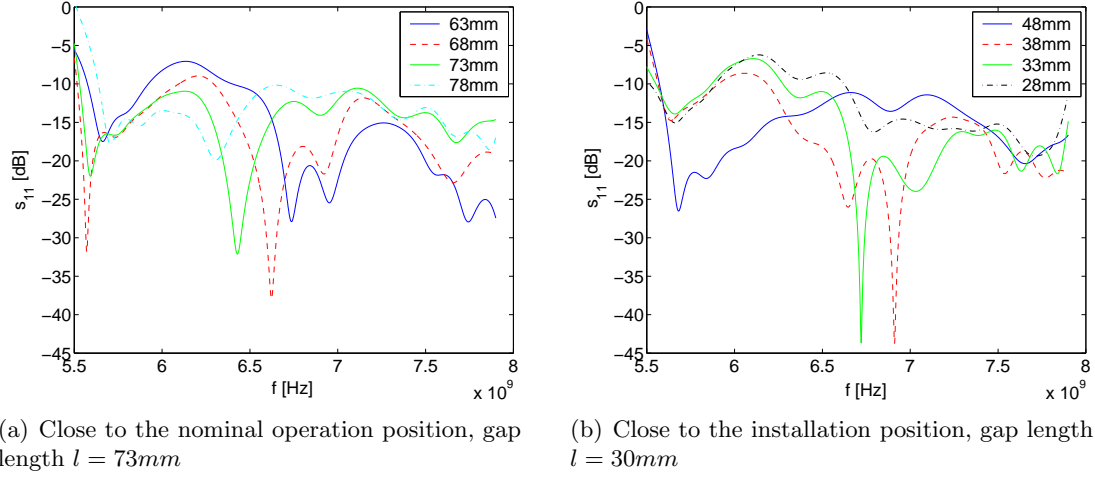


Figure 4.4: The gated s_{11} for different interconnect lengths, measured with waveguide calibration

adapter), the first measurement was repeated after a series of measurements. Again, only insignificant changes in s_{11} were found.

When the length of the interconnect is varied, s_{11} changes considerably. The plot in fig. 4.4(a) shows the reflection factor for four different lengths around the nominal cold length at 20K. There always exists one distinct minimum between 6 and 7GHz, but it moves to lower frequencies for larger gaps. This indicates that the effect is caused by an interference from the two beam-pipe to contact finger discontinuities. The ratio $\frac{l}{\lambda_H}$ stays close to $\frac{7}{8}$, where l designates the length of the gap. It is yet to be determined if this is pure coincidence.

These measurements were repeated for gap lengths close to the position during assembly (@300K). The results obtained were not very consistent, as can be seen in fig. 4.4(b). For intermediate gap lengths ($l \approx 50mm$) we found no distinct minimum at all between 6 and 7GHz. When the l gets close to the position at room temperature ($l = 30mm$), two very deep minima appear at positions that were not really expected. For even shorter gaps the behaviour becomes very bad, e.g. for $l = 28mm$, black chain-dotted line.

It must be stated that the behaviour of the interconnects is not well understood up to now. In most cases there exist distinct frequency ranges, that would be suitable for the reflectometer measurement, even if they are relatively narrow. The reflections depend, however, heavily on the length of the gap. If the properties and the lengths of the interconnects are not sufficiently identical, the valleys of each interconnect may not overlap, resulting in large disturbing reflections from some interconnects. However the results are certainly not final, since the two weldings where the beam-pipes are connected present large discontinuities and the interconnect used is not the most recent type. Measurements on the 50m test track will help to gain further insight.

f [GHz]	6.0	7.0	8.0
group delay [ns]	110	77	67

Table 4.1: Group delay for the 15m section of beam-pipe between two interconnects

parameter	beam-pipe	BNC
group delay	77ns	5.13ns
bandwidth	100MHz	1500MHz
attenuation	$\approx 0.9dB$	@1.9GHz: 0.9dB

Table 4.2: Corresponding parameters of a BNC cable and a 15m beam-pipe section at 7GHz

4.3 Examination of multiple reflections with BNC cables

The effects of the multiple reflections originating from the interconnects were subject to closer examination. We simulated the beam-pipe with its interconnects at distances of 15m by 50 Ω BNC cables of 5ns length. To get relevant results, the beam-pipe's proportions were "downscaled" to the dimensions of the BNC cables. To cover half an arc (1250m), a chain of roughly 100 interconnects (1500m) has to be considered. The relevant parameter for scaling is group delay, which amounts to 77ns for a 15m long section on the beam-pipe at 7GHz (see table 4.1). With the delay of the BNC cables being 5ns (5.13ns including the connectors) we get a scaling factor $sf = \frac{77ns}{5.13ns} \approx 15$.

Since by definition the time domain reflection signal exists just for positive values of time, it can be undersampled by a factor two in frequency. No aliasing will occur this way, unless the reference plane was shifted by doing some calibration. Errors introduced by this calibration may lead to reflections appearing at negative times.

Bandwidth. On the VNA the limiting factor is the resolution in frequency, which is given by the maximum number of points, 1601. The range of 1500m or 100 interconnects corresponds to a group delay of $t_{max} = 7.7\mu s$. For this maximum time we get a maximum frequency step of $\Delta f = \frac{1}{t_{max}} = 65kHz$. Using the maximum number of points we get a maximum bandwidth of not more than $B = 104MHz$. In the following we worked with $B = 100MHz$.

Line attenuation. The attenuation could also be accounted for. This was done by choosing an appropriate frequency range for the BNC cables. Between 0 and 6GHz the attenuation of one cable goes from close to 0dB up to 2dB. By working in a frequency range where one cable presents the same attenuation as 15 meters of beam-pipe, the attenuation can be included into the model experiment.

In table 4.2 the corresponding parameters for the BNC experiment are summarized. In the frequency domain a periodicity with 97.8MHz was observed, which can be interpreted as the Fourier transform of the periodic pulses in the time domain. This frequency corresponds to the electrical length of 5.13ns of one BNC cable with connector as mentioned above.

Figure 4.5 shows the reflection profile from 51 BNC cables in a row, see the mea-

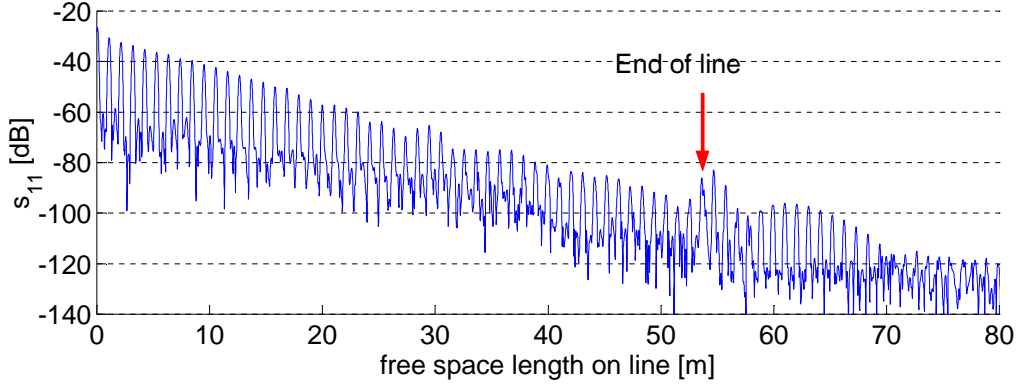


Figure 4.5: Reflections from a chain of 51 BNC cables

surement set-up in fig. C.7(b). Since the bandwidth of 100MHz is rather small, the resolution is not very good. For the first 20 peaks the trace goes down smoothly, afterwards it becomes a bit rough. This is due to the fact that the cables and connectors near the beginning of the line come from one delivery, so they are almost identical. The others are partly from another delivery, partly used cables, which makes a difference that can be seen clearly. At the end of the line we put a matched load. A natural question is then: Where do the later peaks come from?

Well, this is due to the fact that the impedance of the lines and of the load are not exactly 50Ω . The reflections from the connector and the discontinuity added up are larger than one single connector reflection. The later reflections form the “rat-tail” that comes from all the multiple reflections on the line. On the beam-pipe we will not have this problem when trying to look over half an arc, since the waveguide continues beyond the range of our measurement.

Another important fact to notice is the rise of the noise floor between the peaks. At the beginning, the reflections are nearly 30dB above the noise floor, further down the line the noise floor grows by almost 15dB with respect to the peaks’ amplitudes.

Chapter 5

Signal processing

The measurements of the interconnects have shown that in some frequency bands the operation is difficult due to high reflections or attenuation. This implies operation in distinct small frequency bands with some intermediate bands cut out. Furthermore for a given range the VNA's frequency resolution is limited by its maximum number of points, 1601. These constraints inspired us to do some serious signal processing, for which we chose MATLAB[®]. We could improve the final resolution by doing the measurements in subsequent frequency bands on the VNA, transferring the data to a PC and performing the Fourier Transform on MATLAB. This gives also some flexibility in the treatment of the data. Some window functions were examined, a numerical compensation for phase and amplitude distortion and linear attenuation was implemented. The data was displayed in several ways to facilitate their interpretation, and finally some simulations and numerical experiments were carried out.

5.1 The Fourier transform

First of all the data was read into MATLAB by the functions “import” and “multiimport”. The first one performs format conversion from the VNA output file to MATLAB and saves the data in a .mat file for quick access. The latter permits combining data from several measurements in adjacent frequency bands. It checks whether the points on the resulting frequency axis are equidistant and gives an error message if not. Then the data is passed on to the Fourier transform routines which performs windowing, dispersion correction and attenuation compensation. The FFT algorithm requires a power of 2 samples, so a zero padding must be done.

5.1.1 Windowing

A good window suitable for our purpose has got to fulfill the following conditions:

1. narrow main lobe
2. small side lobes
3. very small side lobes far from center

These constraints occur because the resolution in space depends on the width of the main lobe, which therefore has to be sufficiently small. Unlike in other applications,

Window	-20dB main lobe width	side lobe attenuation [dB]	far-away side lobe attenuation [dB]
Kaiser $\beta = 6$	1.24	44	93
Kaiser $\beta = 9$	1.00	66	115
Hanning	1	31	170
Blackman	1.21	58	180

Table 5.1: Comparison of the windowing functions. The main lobe width is normalized to that of the Hanning window

however, the resolution is not of utmost importance, since we do not need to resolve closely spaced peaks of equal amplitudes. What we expect is a periodic pattern of relatively strong reflections from the interconnects, with broad valleys between. The amplitude should fall by roughly 80dB over the full distance of 1000m. To be able to detect a relatively small obstacle close to an interconnect, the main lobe has to be small, but even more important, the side lobes have to be very small to prevent them from being mistaken as separate reflections. The third criterion arises as a result of the large dynamics of the system. It has to be guaranteed that the side lobes of the first reflections are sufficiently small at the position of the last, much attenuated, reflections. Failure to do so will unnecessarily degrade the SNR for the latter reflections, drowning them in the noise floor.

Among the common windows the Kaiser, Hanning and Blackman types were examined more closely (see table 5.1), the Hamming, Bartlett and Chebyshev windows did not reach the finals due to obvious major deficiencies. The three parameters compared are

- -20dB main lobe width, more significant than -3dB width, because interconnects will give some -20dB and we aim at obstacles of -40dB amplitude
- attenuation of the first side lobe and
- far-away side lobes at 80% of the maximum span, with windows 1601 samples long.

The Kaiser Bessel windows that are also used in the network analyser E8358A satisfy the first two conditions very well. By changing the parameter β the shape of the window can be adapted. However, far away from the main lobe the side lobes remain at a relatively high amplitude for low β . For the Hanning and the Blackman window this is not the case, as can be seen in fig. 5.2(b). Increasing the Kaiser β allows further suppression of the far-away side lobes, as well, but for the price of larger main lobes.

The Kaiser window for $\beta = 6$ and the Hanning window have main lobes of almost the same shape and width. The same happens to be true for the Kaiser window with $\beta = 9$ and the Blackman window. These four are plotted in a region close to the main lobe in fig. 5.1. It can be seen that the Hanning window has a quite large first side lobe in comparison to the Kaiser window. Further away from the center however the Hanning window's side lobes go down faster. A similar characteristic can be found in fig. 5.1(b): Again the Kaiser function has lower first side lobes that drop much slower than the Blackman window's. So the Kaiser window is much superior in criterion 2 ("small

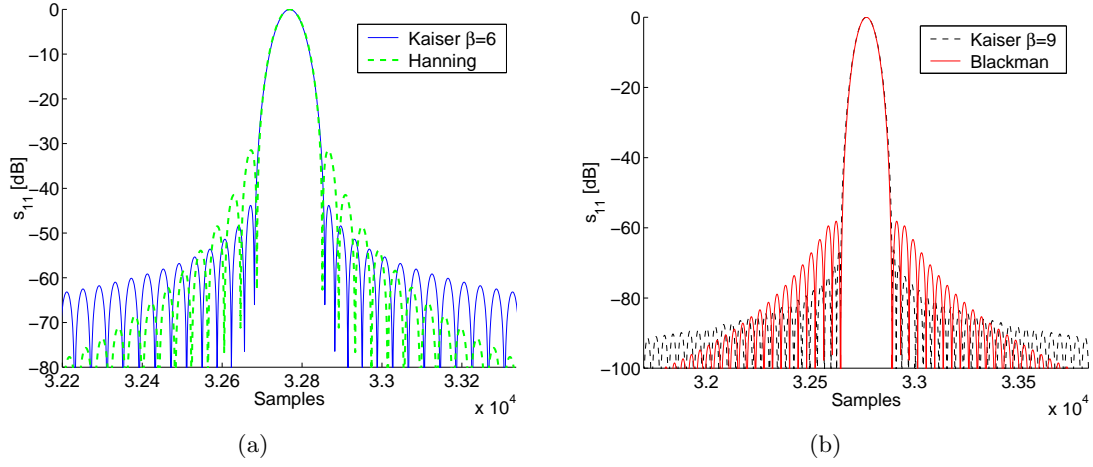


Figure 5.1: The main lobe and the first side lobes of the window functions

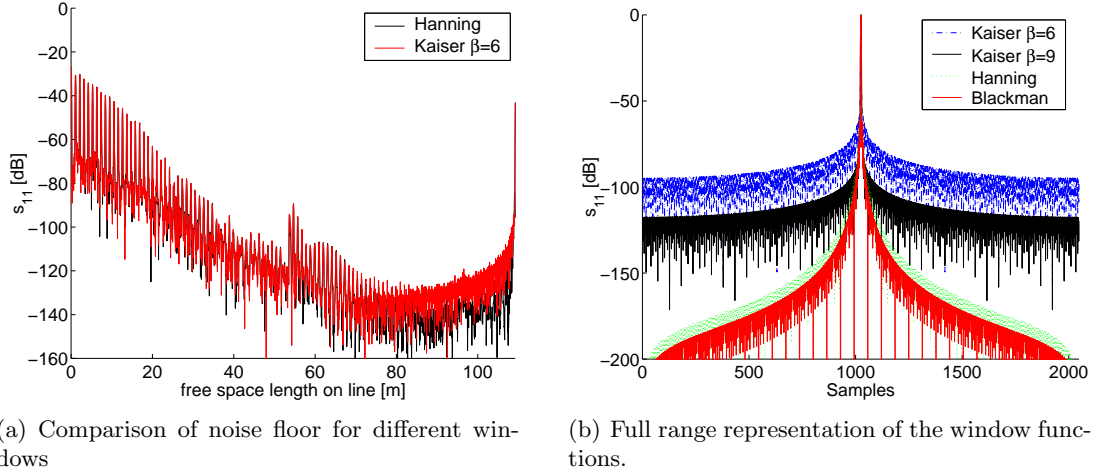


Figure 5.2: Windowing

first side lobes”) but much worse in criterion 3 (“very small far-away side lobes”). This convinced us that the Hanning and the Blackman window were preferable. They should reduce the noise level for larger distances, where it is most critical.

Eventually the Kaiser windows will be used too, especially in case of doubt and for direct comparison with the VNA time domain data. In a test with data from 51 BNC cables simulating 51 interconnects, the impact of high side lobes can be seen very clearly: with a Kaiser window (for $\beta = 6$) the noise level rises considerably for higher distances. This effect is illustrated in figure 5.2(a). A check with the Blackman window that has the highest far-away side lobe attenuation from all the windows available shows still a slight improvement in relation to the Hanning window, but at the price of a larger main lobe.

To put it in a nutshell, the Hanning window seems to be the best trade-off between small main lobe width, small side lobes and high attenuation for far-away side lobes.

5.1.2 Dispersion compensation

As known from many communication systems short pulses drift apart when propagating on dispersive lines. The waveguide being a *very* dispersive media, especially close to cut-off, our pulses tend to be deformed beyond recognition. This is why we needed to compensate for this effect. After having run down z meters on a waveguide with guided wavelength λ_H and cut-off frequency f_c we have a phase of

$$\phi(f) = -\frac{2\pi}{\lambda_H}z = -\frac{2\pi f \sqrt{1 - (\frac{f_c}{f})^2}}{c_0}z = -\frac{2\pi \sqrt{f^2 - f_c^2}}{c_0}z = -2\pi\tau \sqrt{f^2 - f_c^2}, \quad (5.1)$$

introducing the free space delay $\tau = \frac{z}{c_0}$. The group delay defined by $t_g = \frac{\partial \phi}{\partial \omega}$ is described by the formula

$$t_g = \frac{\tau}{\sqrt{1 - (\frac{f_c}{f})^2}} \quad (5.2)$$

The phase can be set to zero for *one* distance z by “focusing” to this distance, i.e. subtracting the above term from the phase of the data. Doing this, however, makes the entire signal shift towards the left, because the entire phase term is removed and the group delay is set to zero. What we really want is to remove phase *distortion*, that is components of higher than first order. This was implemented by fitting a straight line into the calculated phase and subtracting it afterwards. What we get from this is the phase distortion. By subtracting this phase distortion from the phase of the data the focusing is done for one distance z .

This method was tested on data obtained from a C-band waveguide of 8.18m length. The waveguide was built with straight parts and a 180° bend in the middle. The reflections from flanges, the bend and the short circuit can be localized roughly in the plot of the raw data (5.3(b)). The further down the line the longer the pulses become, and this for a length of less the 10m! When focused on the reflection from the short at the end of the line, its shape is quite well reconstituted (see fig. 5.3(b)).

Up to now the dispersion was compensated just in the vicinity of the focus point. By scanning the waveguide with the focus running from the beginning to the end of the line the entire plot can be focused. This gives lots of more or less redundant data, because the area far from the current focus is so blurred that it isn't of much use. We did however keep this information and displayed it in a 2D plot (fig. 5.4(a)). The amplitude of s_{11} is coded in color and the traces are stacked for ascending focusing length.

This kind of representation has some major advantages: First, it's colored and nice to look at and second it helps finding out a peaks provenience. This is possible because we can benefit from the redundancy in the plot. Each peak is in focus just for one trace. When we move up or down on the plot it runs apart. The focusing length is different for each mode, as it depends on the dispersion and therefore on the cut-off frequency. So it can be easily verified if a peak comes from the desired mode by checking whether it is in focus on the diagonal or not.

After this inspection it is more interesting to see just the focused data that lies on the diagonal. In fig. 5.4(b) this data is plotted together with the points that were actually in focus. The corrected data was obtained by cutting out the focused region from each

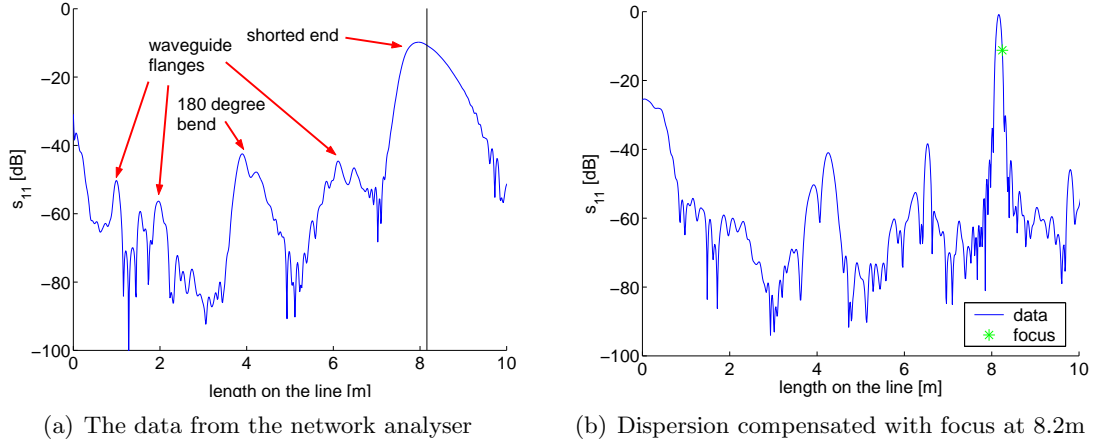


Figure 5.3: Effect of dispersion on a C-band waveguide

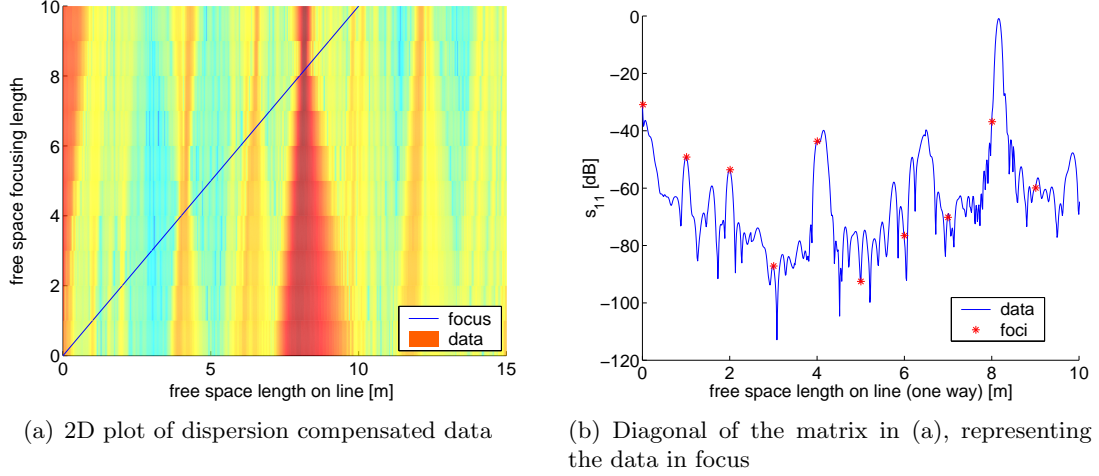


Figure 5.4: Dispersion compensation

trace of the plot on the left. For sufficiently small focusing step widths the effect of waveguide dispersion can be almost perfectly compensated. Compare the resolution of the focused trace to that of the raw data in fig. 5.3(a)!

5.1.3 Attenuation compensation

As with the phase in waveguides the amplitude suffers some distortion as well. Unlike phase distortion however, it does not only depend on the cut-off frequency, but also on the mode and the waveguide geometry. The attenuation for the first TM and the TE modes was given earlier in the equations 3.4 and 3.5, however amplitude distortion is much less critical than dispersion. In our range of operation, not too close to cut-off, the difference between the minimum and maximum attenuation in dB is in the order of a few percent. For short distances (e.g. 10m) this effect is negligible, but for longer distances it will have a perceptible impact. Full attenuation compensation needs the same approach as full phase compensation, namely setting the focus subsequently to short sections and piecing together the data at the focus. This method was implemented

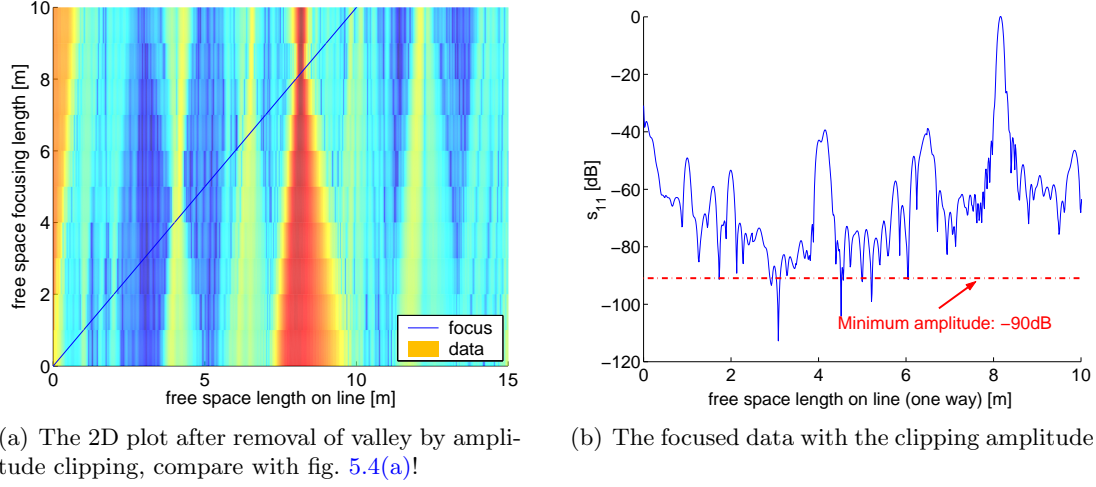


Figure 5.5: Amplitude clipping

and tested for the $TE_{\square 01}$ mode on the C-band waveguide.

For non-dispersive media a simplified version of attenuation compensation can be used: the time-domain signal has just to be multiplied with an exponential term. The data obtained from measurements on the coaxial line was corrected this way.

The advantage of doing attenuation compensation is basically that some of the signals properties can be analysed more easily. The deterioration of the SNR for points further down the line e.g. can be judged directly by looking at the rising noise floor, especially for plots where the amplitude information is coded in color we got a much better resolution.

Another trick allowed us to improve the resolution in the 2D focusing plot. Usually the Fourier transform signal shows some very deep pits. By clipping the amplitude of the deepest valley to a minimum value, we get better resolution of the small peaks without losing relevant information, as illustrated in figure 5.5. More elaborate features such as zooming into a certain amplitude range in the 2D plot have yet to be implemented.

5.2 Simulations

5.2.1 Multiple reflections by the interconnects

After the first reflection measurements on an interconnect it became clear that some additional work would be necessary to master the problems with multiple reflections between the interconnects. There are two major questions:

1. How large is the power loss due to the reflections?
2. Is it possible to measure a reflection from one interconnect in spite of all the superposed multiple reflections?

Both questions depend essentially on one parameter: $r = |s_{11}|^2$, the power reflection coefficient from one interconnect. The first question is not hard to answer:

The power getting through N interconnects is just $1 - (1 - r)^N$. To investigate the impact of r on one single reflection, a routine in MATLAB was written that allows it to

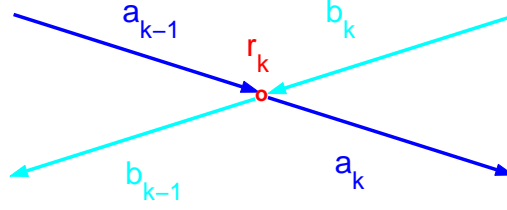


Figure 5.6: Reflection of the forward and backward running waves on an interconnect

follow the pulses propagating down a line with periodic interconnects. The signal can be interpreted as being sampled at the position of each interconnect. This allows us to formulate recursions for the forward and backward running wave a_k and b_k on the line (fig. 5.6):

$$\begin{aligned} a_k &= a_{k-1}(1 - r_k) + b_k r_k \\ b_{k-1} &= a_{k-1} r_k + b_k(1 - r_k) \end{aligned}$$

with the index for time or space k and the reflection coefficient of the k^{th} interconnect, r_k . Note that $\mathbf{a} = (a_k)$ and $\mathbf{b} = (b_k)$ are vectors of length $N + 1$ for N interconnects, describing the waves running on the line, the same as $\mathbf{r} = (r_k)$ describes the reflection coefficients of all the interconnects on the line. For identical interconnects we have $r_k = r \ \forall r \in \mathbf{N}$. At the time k , the reflections coming out at the beginning of the line $\mathbf{s}_{11} = (s_{11,k})$ and the transmission going through $\mathbf{s}_{21} = (s_{21,k})$ are then given by

$$\begin{aligned} s_{11,k} &= b_1 \\ s_{21,k} &= a_N \end{aligned}$$

It was assumed that the divers reflections add up in power, like noise. As we have many reflections of different amplitude and phase, this should be true as a first approximation.

Fig. 5.7 shows two outputs of the routine. On the left end of the line (length: 10 samples) an input pulse with amplitude 100dB was injected. It propagates down the line and provokes a reflection at every interconnect on the left side in fig. 5.7(a). When the backward travelling wave reaches the end of the line, it manifests itself as a reflection, plotted over time on the right side of 5.7(a).

After 10 steps the pulse arrives at the end of the line and a transmitted pulse is first observed (see fig. 5.7(b) on the right side). On the line itself there are still waves travelling in both directions, which causes the “rat-tail” in the s_{11} and s_{21} plot.

So what happens now when the pulse has to travel over 70 identical interconnects corresponding to $\approx 1000m$ on the beam-pipe? This case was simulated for different reflection coefficients, the results are plotted in fig. 5.8. The interconnects were assumed to have identical properties. The amplitude of the direct reflection, the main reflection, decreases linearly in the logarithmic scale, while the decrease of the total reflection s_{11} is much more slower for large r . The effect of the multiple reflections is even more visible for the ratio $\frac{\text{main reflection}}{\text{rat-tail}}$, where the rat-tail stands for $s_{11} - \text{main reflection}$,

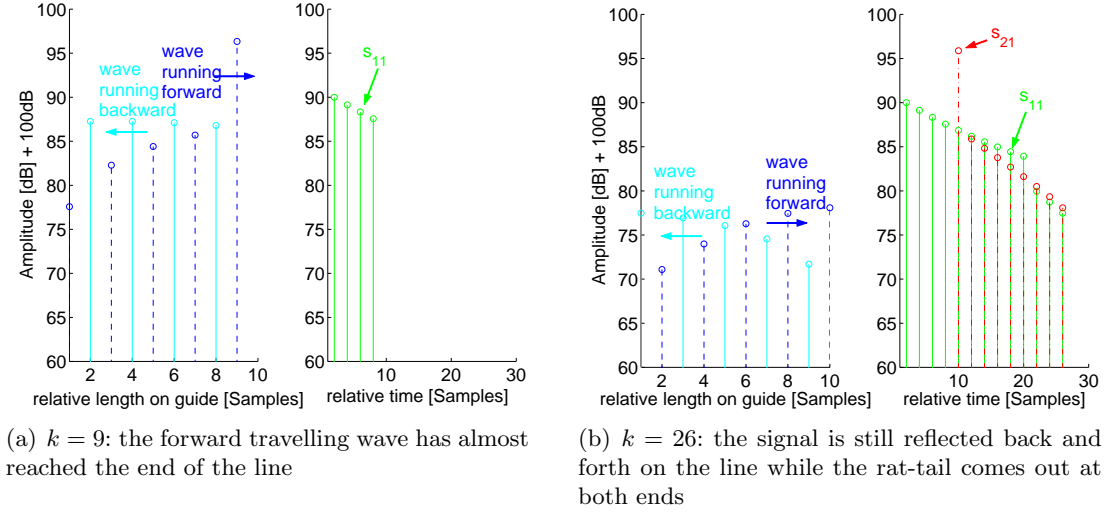


Figure 5.7: Simulation of multiple reflections on a line of length $N = 10$ samples with $r = -10\text{dB}$

so everything apart from the main reflection. This ratio can be considered as kind of SNR for the main reflection. In the region of $r \approx -20\text{dB}$ the altogether s_{11} reacts in a very sensible way to small changes. A decrease of r by 3dB makes the SNR rise per 6dB, while an increase of 4dB makes it fall by 11dB, and the main reflection disappears in the rat-tail. If r stays below -20dB, the main reflection should be quite easily distinguishable, as the simulation shows that it will be 6dB above the sum of the multiple reflections.

For the simple case of identical reflections, the problem can easily be treated analytically. The results are in perfect agreement with those obtained by the simulation. The amplitude of the main reflection is especially easy to check, its value is given by $r(1 - r)^{2(N-1)}$, with N denoting the number of interconnects. The sum of all the multiple reflections having undergone *exactly* three reflections has a magnitude of $\binom{N}{2}r^3(1 - r)^{2(N-2)}$. For small r and not too large N the reflections of higher order can be neglected and it follows $SNR \approx \frac{2}{N^2r^2}$. The condition for the “rat-tail” to be negligible is therefore $\frac{2}{N^2r^2} \gg 1$. For 70 interconnects this condition holds roughly for $r < 0.01$ or $r < -20\text{dB}$, as was confirmed by the simulations.

In reality we do not really expect to find identical reflections from each interconnect. This is why we examined more general cases, first one single strong reflection that could come from a contact finger reaching into the beam-pipe among small ones. Afterwards a random distribution of the values of \mathbf{r} with logarithmic mean $\mu_{\mathbf{r}}$ was examined.

The strong reflection does not change much the shape of the curves; it essentially causes one large reflection and lower reflections afterwards due to the power masking (see fig. 5.9(a)).

For the randomized distribution we used a normal distribution on the log amplitude, thus in dB, as this seems more realistic than a linear amplitude normal distribution. The mean of this distribution calculated using the linear amplitudes is higher than the logarithmic mean, so the amplitude of the later reflections and also the SNR decreases. For a standard deviation of 3dB, plotted in fig. 5.9(b), some far-away reflections already fall beneath the noise level. For smaller variations of \mathbf{r} the effect is less disturbing, but

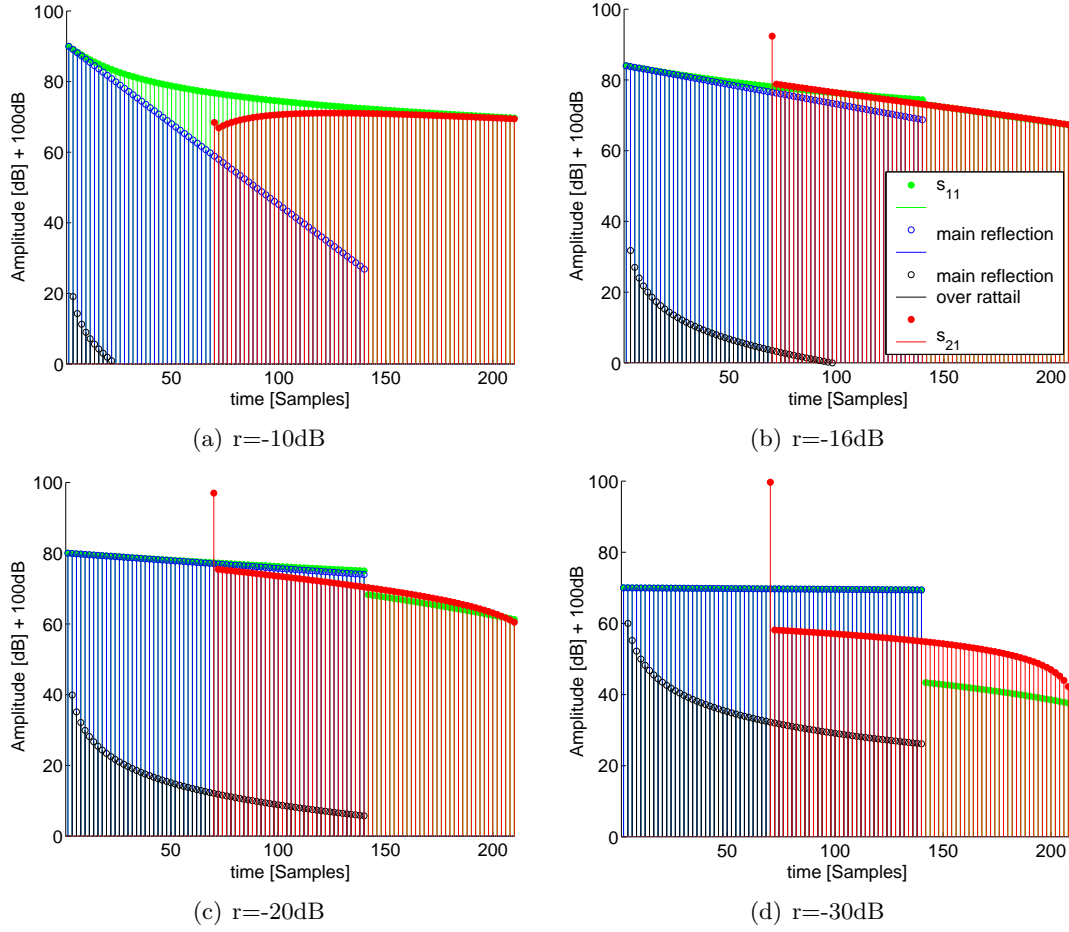


Figure 5.8: Simulation of multiple reflections over 70 interconnects in dependence of the reflection coefficient r per interconnect. The solid black trace, the lowest in each plot, depicts the ratio $\frac{\text{main reflection}}{\text{rat-tail}}$, denoted as SNR in the text. Unlike for the other traces the values on the vertical axis correspond to the amplitude [dB], not the amplitude [db]-100

again we see that a sufficiently low μ_r in the range of operation is of great importance. Finally, note the smoothness of the rat-tail in fig.5.9(b): Since it is the sum of many small components, the random distribution of r does not have a large impact.

5.2.2 Mode mixing

There is no doubt that mode mixing will be observed on the beam-pipe to a certain extent. There are no means to avoid the excitation of other modes at discontinuities, but their impact can be minimized. The most practical way since already implemented is by doing dispersion compensation. If the other possible modes have different cut-off frequencies than the mode used, dispersion compensation will work just fine for this distinct mode, while the other modes will stay more or less smeared out, depending on how far their cut-off frequencies are from the desired mode.

The simulation was run for a situation that will be encountered in the beam-pipe:

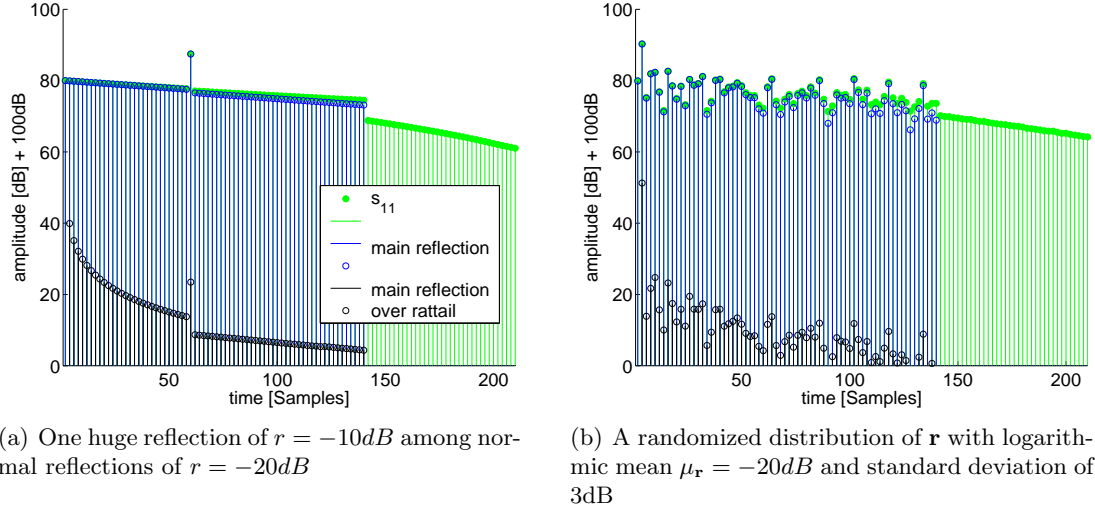


Figure 5.9: Simulation of more general cases, over 70 interconnects

The desired TM mode ($f_{c1} \approx 5.3GHz$) is disturbed by the fundamental TE mode ($f_{c2} \approx 3.6GHz$). Fig. 5.10 shows the results obtained on a shorted line of length 8m. Without phase compensation the reflection from the TE mode is much narrower, as it is further from its cut-off and therefore suffers less distortion. The dispersion compensation was set to correct for distortion of the TM mode by choosing the TM mode's cut-off frequency for correction. When the focus of dispersion compensation is moved, the TE peak does become much sharper, but it is focused for the wrong focusing length, namely too early, as it sees a “bad” compensation function. For larger focusing lengths it gets smeared out again, with the known asymmetric shape, but now the tail is on the left side, caused by an “overcompensation” of phase distortion.

For the TM mode things look different: as the focus approaches, its peak gets sharper and sharper, as expected. By checking if the peak reaches its maximum at the right moment it can be identified as the TM peak.

A second simulation tested how good the suppression of a bad peak falling onto a peak of interest works. For that purpose the propagation of the different modes on a line with two discontinuities provoking a reflection of 0dB in each case was simulated. The cut-off frequencies were set to $f_{c1} = 5.3GHz$ (TM mode) and $f_{c2} = 3.6GHz$ (TE mode), while the frequency band spanned from 6 to 7GHz. The discontinuities were situated some 15m down the line so that the two reflections fall on the same place in the s_{11} seen at the beginning of the line. Figure 5.11(a) shows the simulated raw data where the “bad” peak is much sharper than the other one. After focusing onto the TM mode the “bad” peak is smeared out while the desired peak rises well above the other one (fig. 5.11(b)). Considering the maximum amplitude it can be seen that the unwanted mode's peak amplitude decreases by 10dB, while the focused mode's peak rises by roughly 10dB, so we have got a “bad mode rejection ratio” of 20dB. The distances of the discontinuities will be much longer on the beam-pipe, which will still increase the smear-out of the undesired modes. On the other hand it will be difficult to measure over a frequency band 1GHz wide, which could well entail negative effects. Both spatial resolution and the bad mode suppression improve with growing bandwidth.

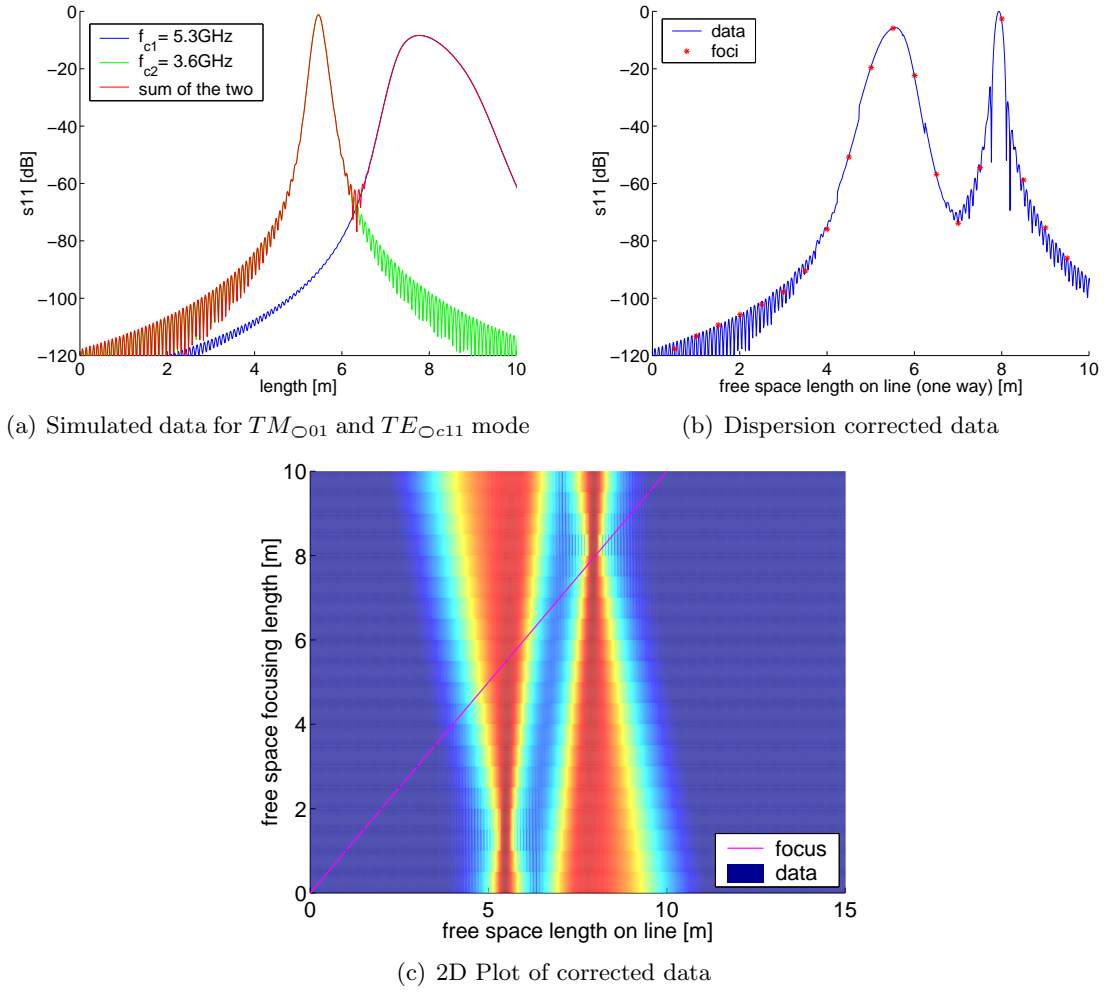


Figure 5.10: Simulation of mode mixing with two modes

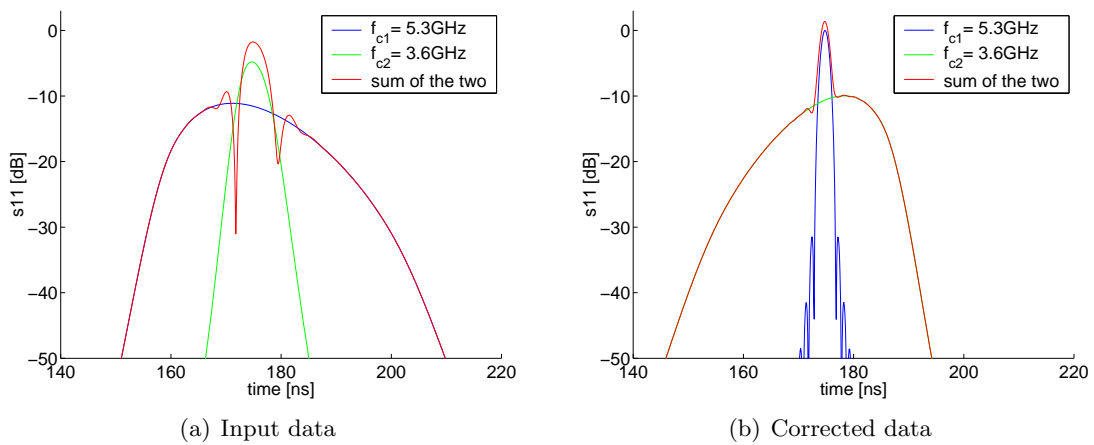


Figure 5.11: Simulated data from two peaks of two different modes falling on the same spot. Note that after dispersion compensation the symmetry of the broad peak changes. First it was the uncompensated TM peak and afterwards it is the overcompensated TE peak

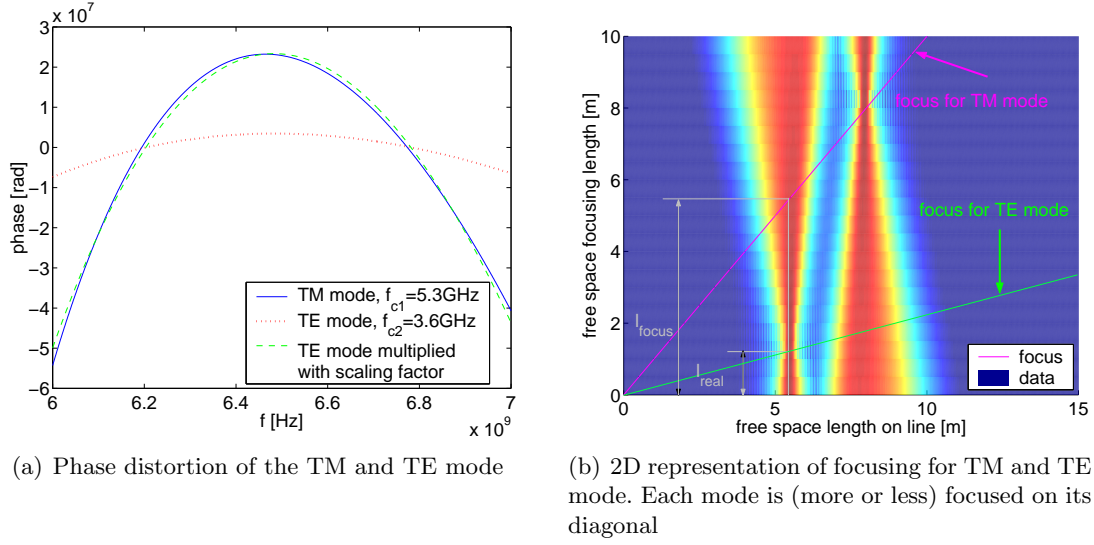


Figure 5.12: Focusing of desired and undesired modes

Calculation of the relative focusing length for undesired modes. It was observed above that undesired peaks are considerably sharpened for certain focusing lengths. While the TM peak with $f_{c1} = 5.3\text{GHz}$ was in focus at approximately $l = 8\text{m}$, the TE peak with $f_{c2} = 3.6\text{GHz}$ was focused much earlier already, for nearly $l = 1.5\text{m}$ (see fig. 5.10). This can be explained by considering the phase distortion of the two modes. Both are of very similar parabolic shape, the TE curve is roughly a scaled version of the TM curve (fig. 5.12(a)). The Taylor series development of the phase contains only terms of f^{2n} with a non-negative integer n . Keeping in mind that the focusing routine multiplies the phase distortion of the TM mode by the time shift τ , it is obvious that the TE mode will be in focus for some much too small τ (see formula 5.1), this way it should be possible to get a hint on a reflection's origin.

In a small script the magnitude of this deviation is calculated by MSE approximation and corrected for different mode propagation velocity. A relative parameter k_{rel} is obtained this way that gives the ratio of $\frac{l_{focus}}{l_{real}}$, with l_{focus} designating the focus length used for dispersion compensation and l_{real} the observed real focus length. This is illustrated in fig. 5.12(b), together with the two diagonals on which each mode is approximately in focus. By drawing the diagonals in the 2D focusing diagram it is very easy to identify the origin of each reflection, however this concept is somehow compromised by the fact that mode mixing can arrive several times, with echos falling onto none of the diagonals. However we can be quite sure that a reflection falling on the main diagonal comes from the desired mode.

Chapter 6

Measurements on the “50m” test track

The results of all the experiments and calculations up to this point were quite promising. The attenuation was determined experimentally by resonator measurements and checked with values obtained from theory for similar waveguide profiles. The impact of the multiple reflections was examined with the BNC line experiment and a simplified version of the problem was simulated in MATLAB. Both dispersion compensation and mode mixing were studied on a C-band waveguide and on synthetic data processed on the PC.

All these tests are well adapted for studying the influence of each effect separately. However, in reality we have to deal with all these problems *at once*. The following developments lead us one step further towards the ultimate aim, which is the measurement of a complete LHC cold arc.

The test track has a length of approximately 44.2m including two interconnects, the first at 14.0m and the second at 29.7m. See some pictures in the appendix, figures [C.8\(a\)](#) and [C.9](#). The assembly was made to be as similar as possible to the LHC. The major differences are:

- There was no cold bore installed around the beam-screen. This made the assembly much lighter and allowed us to insert and retrieve obstacles. However because of that the attenuation of the waveguide modes, especially the TE modes, could be different in the LHC machine.
- The interconnects were slightly different, worse from our point of view, from those that are actually planned to be installed in LHC
- The samples of beam-screen used had minor deficiencies. However, those should not strongly influence their behaviour at high frequencies

The default length of the interconnects was set to be within the specs of the operational position. To provide sufficient mechanical stability, the beam-pipe and the interconnects were fixed with supports at 12 points so that the vertical sagging never exceeded 5mm. All measurements were performed with the Agilent E8358A network analyser and for the coupling to the waveguide a conical waveguide adapter equipped with different mode launchers was used.

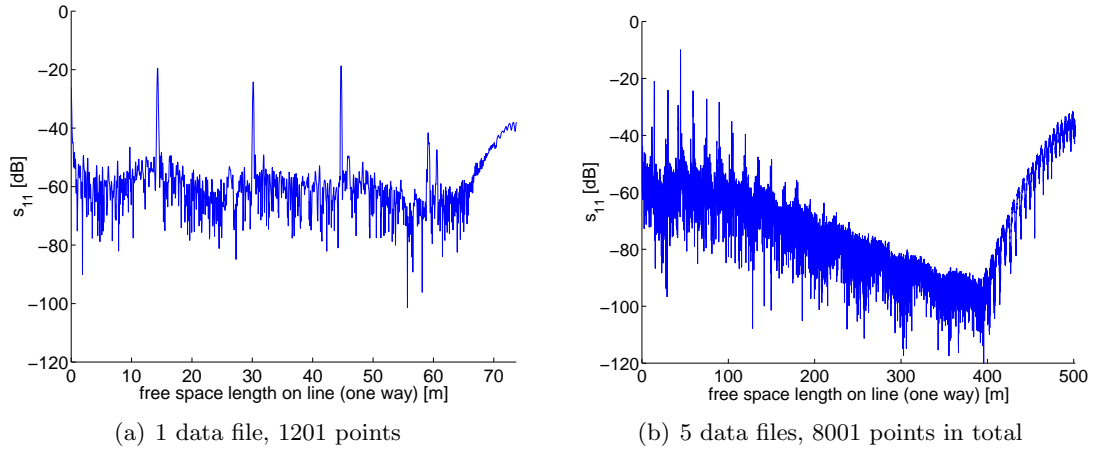


Figure 6.1: Increasing the range by appending multiple measurements, focused data

6.1 Performance of the actual signal processing

The main tasks of the signal processing routines are:

- Make it possible to use more than the maximum number of 1601 points given by the VNA, thus providing sufficient resolution and range
- Compensate waveguide dispersion
- Give a nice graphical representation of the results to allow recognition of detrimental effects such as mode mixing and multiple reflections
- Lower the noise floor by external trace averaging

Increasing spatial range. To cover half an arc in reflection mode, we need to measure with a bandwidth of less than 100MHz to avoid aliasing (with 1601 points). Therefore, in order to get good spatial resolution, the frequency band has to be stepped through by doing multiple measurements. The “multiimport” routine loads the files and makes up one data vector from raw data. Figure 6.1 shows the evaluation of measurements in a range between 6.0 and 7.5GHz. In the left image data from just one trace with 1201 points is depicted, and with this resolution it can be seen that the range is less than 100m.

On the right data from 5 measurements in adjacent frequency ranges has been used, giving an effective increase in range of $\frac{8000}{1200} = 6.67$, as can be seen in the image. The tail coming in from the right in both pictures is a residue from the numeric focusing. This is due to the fact that the FFT is a cyclic operation. When the focus comes close to the end of the time axis, the first pulses are treated as very defocused reflections. They are smeared out, with a part of the power spreading towards negative time, thus showing up on the right end of the time axis.

Performance of dispersion compensation. As we have seen already for the C-band waveguide dispersion compensation is a very important procedure. For the lengths of line we are dealing with compensation becomes indispensable, at least when

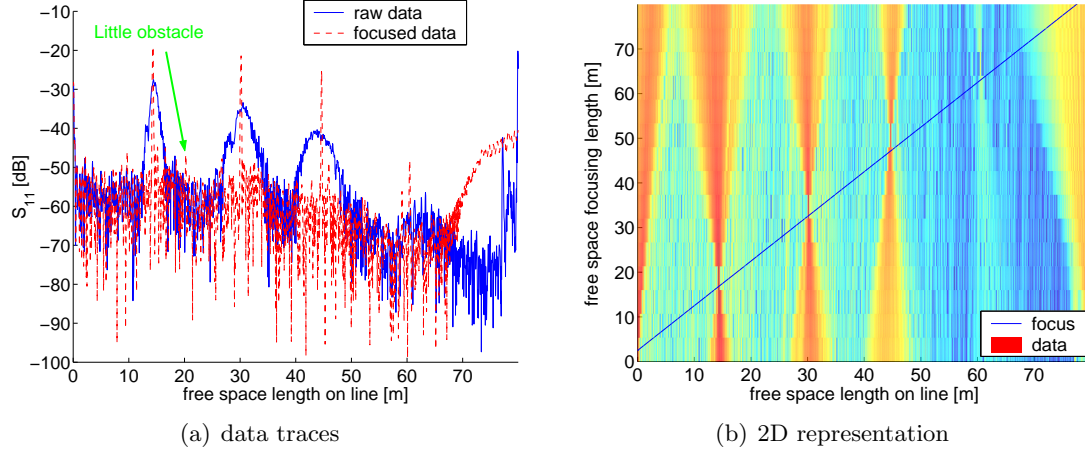


Figure 6.2: Dispersion compensation for the first TM mode on the test track

working with frequency bands wider than 100MHz. The plots in fig. 6.2 show the results of a measurement between 6.0 and 7.9GHz, obtained with waveguide calibration for the first TM mode. Due to the rather large bandwidth, the dispersion causes a very important smear-out, only the interconnects and the load at the end can be recognized. The corrected data on the other hand allows the observation of many more details, e.g. the test obstacle, a wire of 1mm diameter, sticking 5mm into the beam-pipe at $l = 20m$. The compensation routine seems to work properly, apart from one little problem: In the 2D representation (fig. 6.2(b)) the diagonal does not really pass through the foci of the peaks but rather drifts off downwards. This problem is inherent to our correction method. We have to assume some frequency response for the reflection to be focused. This frequency response however is not known beforehand, as we principally do not know what objects we may find in the beam-pipe. For the interconnects the response could be measured, but it depends on many factors, especially the mechanical length. For the sake of easy implementation the dispersion compensation is done for the response of an ideal short. The remaining error seems to be due to non-ideal shorts and not perfect calibration.

A similar problem is the exact determination of a reflection’s position on the line. Here the group delay in the operational frequency range comes in. If the correction is well done, the pulse should not shift in time and the only problem persisting is to calculate its position in space from its position in time. As the group delay varies with frequency, the delay of a pulse (=wave packet) must be some mean of the group delays of all the frequencies that make up the pulse. Again the unknown frequency response of the reflection comes in. To find the most appropriate mean we chose as Ansatz the general mean of order α for an N -element vector $\mathbf{x} = (x_n)$

$$\mu_\alpha = \left(\frac{\sum_{k=1}^N x_k^\alpha}{N} \right)^{\frac{1}{\alpha}} \quad (6.1)$$

The best match for the experimental data was found for $\alpha = -2$. An eventual theoretical explanation for this empirical result has yet to be found.

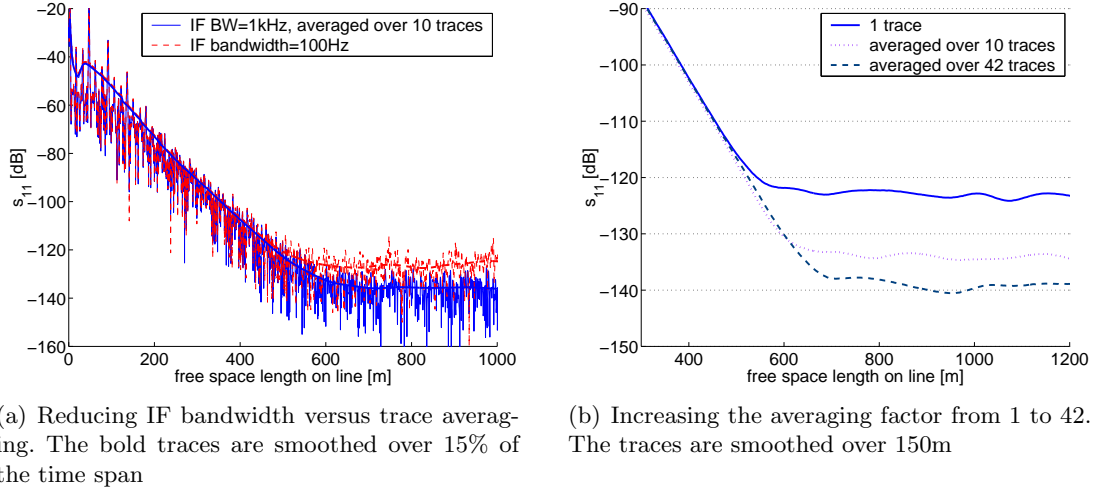


Figure 6.3: Increasing the dynamic range by reducing IF bandwidth and by trace averaging

External trace averaging. When doing measurements requiring very high dynamic range on a network analyser, there is the choice between several strategies. First the bandwidth of the IF filter should be reduced as much as possible to reduce the noise level. On the E8358 the IF bandwidth can be set as narrow as 1Hz. However, it was observed that, presumably due to drift errors and distortion by the IF filter the noise level did not decrease much when going below 100Hz.

Another strategy consists in averaging the data from many traces, either in time domain or in frequency domain. This should not make any difference since the Fourier transform is linear. This option allows reducing noise errors while avoiding the effects of amplitude drift.

A more theoretical approach is presented in [16]. Introducing the drift constant T_D (time during which the drift error does not change much) and the scan time T_{sc} (time to measure one trace) it is deduced that for averaging over N traces

- when $NT_{sc} \ll T_D$ the drift rate is nearly constant over the overall period NT_{sc} and therefore the averaged drift error is nearly the same as for only one trace.
- On the other hand when $NT_{sc} > T_D$ but still $T_{sc} \ll T_D$ the drift error will eventually change sign and the overall drift error after averaging will be smaller than for one scan.

Trace averaging is implemented on the network analyser, but the results were not very satisfactory when it came to maximizing dynamic range. We could only make suppositions about why this was the case (numerical round-off errors?!), so we tried another approach. The raw data was exported to the PC, and trace averaging was done externally. For this purpose we made 10 measurements of an identical set-up using an IF bandwidth of 1kHz and compared it to the result of one trace taken with an IF bandwidth of 100Hz. The results are illustrated in figure 6.3.

Reducing the IF bandwidth from 1kHz to 100Hz reduces the noise floor a little (not shown in the image). However when averaging 10 traces, each taken with an

IF bandwidth of 1kHz, the noise floor decreases much more (fig. 6.3(a)). In fact the improvement is close to the 10dB predicted by theory. This observation encouraged us to try to further reduce the noise floor by increasing the averaging factor. For 42 traces we still found an improvement of approximately 5dB, compared to the theoretical reduction of just $10\log(\frac{42}{10}) \approx 6dB$ (see fig. 6.3(b)). It must be checked, possibly by automated measurement, if further improvement is possible and at which level the noise floor converges. The peaks rising above the mean are up to 9dB above the noise floor for an averaging factor of 10. With the maximum amplitude of the reflections of -20dB (for fig. 6.3(b)) we find for an IF bandwidth of 1kHz a dynamic range¹ of

- 94dB for one single trace
- 105dB for averaging over 10 traces and
- 110dB for averaging over 42 traces.

Most probably both increasing spatial range and trace averaging, will have to be applied. Further tests have to be carried out to determine how they influence each other. Increasing the number of points by doing several measurements naturally increases the measurement time. Taking time drift into account this may deteriorate the dynamic range. Multiple trace averaging can compensate this effect, however the total measurement time should not exceed a few minutes.

Let’s do a quick estimation: Taking one trace with an IF bandwidth of 1kHz and 1601 points takes 1.6s. To get good spatial resolution let’s assume a total bandwidth of 1GHz \Rightarrow 10 sweeps with 100MHz bandwidth \Rightarrow 16s for one sweep over the entire frequency band. If we want to reduce the noise floor by 10dB, we need to average over 10 traces, so the total measurement time rises to 160s. Taking a few minutes time for one measurement should not pose much a problem, so this scenario seems realistic.

For longer periods however other kinds of drifts etc. may enter into the game and on all accounts the device simply gets impractical. So we can state that there will be a trade-off to find between good spatial resolution (large number of points) and low noise floor (large averaging factor), the limiting factor being the total measurement time.

6.2 Attenuation

In the previous chapters much effort was devoted to determining accurately the attenuation of the waveguide modes. In the resonator not necessarily all the effects would yield a measurable attenuation. Coherent scattering from the slots e.g. would just act like a reactance and lead to a detuning of the modes. On the test-track we had the possibility for the first time to observe directly the cumulated effect from wall resistance, slots, interconnects, etc. Since we had just one waveguide adapter at hand, a direct measurement of s_{21} was not possible. Therefore we switched to reflection mode and put a short-circuit in the form of a brass plate at the end of the beam-pipe. The response was analysed in two ways:

1. The pulse coming from the end was gated on the network analyser to get the frequency response. Even though the pulse had suffered a huge smear-out, this

¹difference of maximum amplitude to peaks of noise floor in time domain

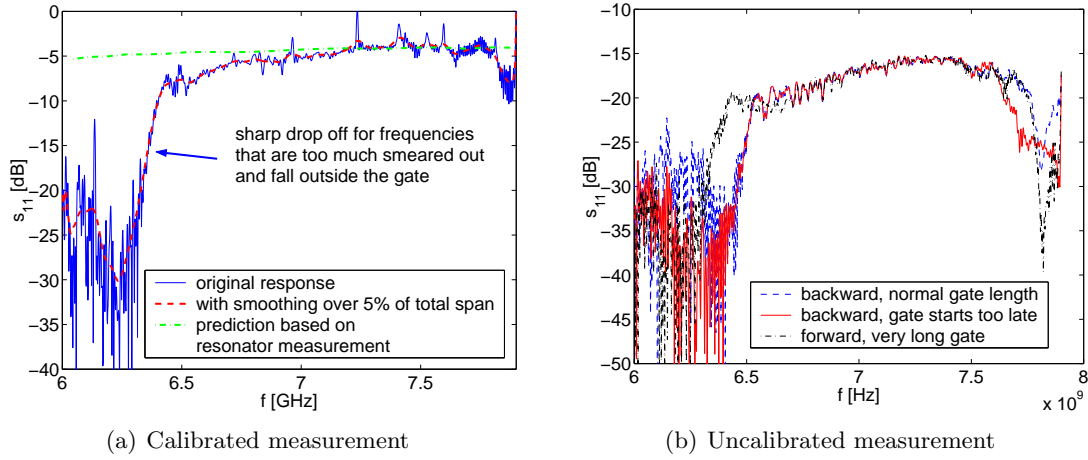


Figure 6.4: A short, measured through 44m of beam-pipe, after time-domain gating

should not change the magnitude in the frequency domain, since dispersion acts just on phase.

2. Dispersion compensation was run on the data and the amplitude of the pulse from the short was evaluated in time domain.

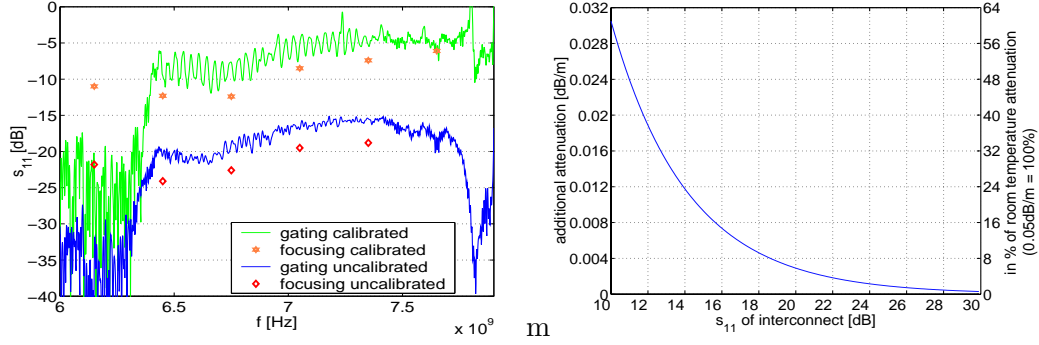
Time domain gating of the short’s response. Fig. 6.4 shows the pulse from the shorted beam-pipe, gated in time domain. On the left the measurement with waveguide calibration is compared to the attenuation measured with the resonator method. With the attenuation of roughly 0.05dB/m found earlier, the two-way loss over 44m should therefore be close to 5dB. Indeed we found a very good agreement for frequencies in the range of 7.2 to 7.8GHz. For lower frequencies the magnitude falls slowly and below 6.5GHz the gated response goes down sharply. This is definitively due to gating, as can be easily understood:

The group delay grows for lower frequencies. When gating is applied, the tail of the pulse has to be cut off somewhere, all the frequencies which arrive later fall out of the gate. The sharp peaks in the solid blue trace come from imperfections of the calibration, as has been verified by checking with a short from the calibration kit.

In the plot on the right side (fig. 6.4(b)), results of uncalibrated measurements are shown. The shapes of the curves are very similar to those on the left, just shifted downwards by roughly 12dB. This indicates that the excitation element works almost equally good – or equally bad – for the entire frequency range. Residues of the calibration cannot be found.

To check the validity of the results, the measurement on the test track was performed in the both directions: first we looked in from one end with the short fixed at the other end and afterwards we did it the other way round. The respective curves match very well.

There is still another effect that was examined: the influence of gating. On the Agilent network analysers gating is implemented in such a way that the frequency response in the center is very close to the real value while towards the edges large errors are possible. As a rule of thumb, the 10 to 20% close to the edges cannot be taken seriously. But due to dispersion the high-frequency components make up the start of a pulse



(a) Comparison of time domain gating to focusing of a short done in 300MHz wide frequency bands. (b) The additional attenuation by power scattering from the interconnects

Figure 6.5:

while the lower frequencies can be found in the tail. Therefore, when the beginning of the pulse is cut away, the high frequencies suffer most (solid red trace in 6.4(b)), while a larger part of the low frequency components are captured for very long gates (dash-dotted black line).

Dispersion correction of the short’s response. This is the most straightforward method: The data was taken from the network analyser and fed into the focusing routine. In the corrected data trace the magnitude of the reflection from the short can be read off directly.

However, using this method the magnitude of the short’s reflection seems to be underestimated. In figure 6.5(a) the data of gating and focusing are compared. It can be seen that, independent of measuring with or without calibration, the focusing gives systematically a value about 3dB too low for the short’s reflection. It is not entirely clear why this happens. But, as pointed out before, the focusing may be off-diagonal, thus not giving the maximum value. For very sharp peaks like from a short-circuit this may lead to a significant discrepancy. Similar comparisons for smaller reflections originating from the interconnects showed very good agreement between gating and focusing (within 1dB). On the other hand it cannot be entirely excluded that this may be due to some yet undiscovered effect or even bug of the focusing routine.

6.3 The interconnects

An entire chapter has been devoted to the evaluation of the interconnects’ impact. However in the latest measurements on the test-track it became apparent that the behaviour of the interconnects can not be determined adequately when the section of beam-pipe on both ends is not long enough, that is, in the order of meters. There is one problem with the material at hand: none of the interconnects used are the type which will be installed in the LHC. Furthermore some minor changes were made to allow easy assembly. The interconnect used above should therefore have significantly different properties. However it has to be emphasized that the results presented below may be somewhat pessimistic and are not final. Certainly the interconnects will not stress our

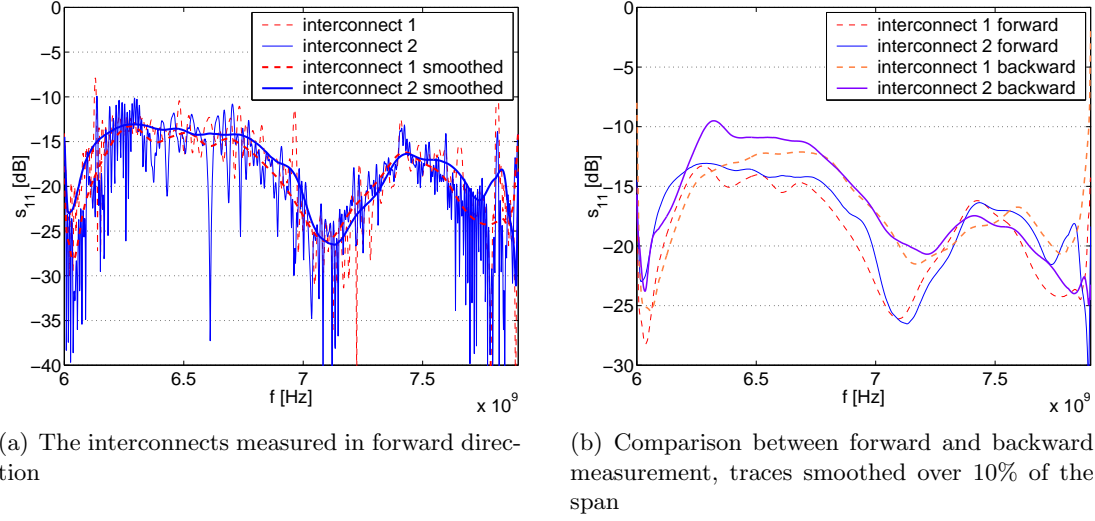


Figure 6.6: Calibrated measurement of the interconnects in reflection mode, corrected for the line attenuation by 0.05dB/m, after time domain gating. Both interconnects are close to the operational position. The results are preliminary, since the interconnects used are not the latest design and were slightly altered for practical reasons

system’s attenuation budget for operation at room temperature. Fig. 6.5(b) shows the additional attenuation α_{add} by power scattering by the interconnects, calculated with the formula

$$\alpha_{add} = -10 \log(1 - 10^{\frac{s_{11i}}{10}}) / 15 \quad [\text{dB/m}] \quad (6.2)$$

for the reflection s_{11i} per interconnect and an interconnect spacing of 15m. For reasonably small reflections, e.g. below -18dB, this effect should come up for less than 10% of the resistive losses at room temperature. It’s another story to be able to distinguish one interconnect’s response through many others, as will be pointed out later.

In the figure 6.6 the preliminary results are presented. Since the data was gated in time domain, the outermost 10% of the frequency axis have to be ignored. On the left plot a large distinct valley going down below -25dB can be seen in the response of both interconnects. Some of the peaks in the original response come from imperfect calibration. So far the behaviour seems quite satisfying. Something really unexpected happens when the measurement is performed from the other end (see fig. 6.6(b)). The behaviour changes radically, with much higher reflections being observed over almost the entire frequency range. This can be understood when considering the asymmetrical structure of the interconnect.

In the draft in fig. 4.1 the forward measurement corresponds to looking from the right side, where the contact fingers are welded onto the beam-pipe. There should be two major reflections as we have two discontinuities: One from the sliding contact on the left and another from the place where the contact fingers are welded onto the beam-pipe. When the amplitudes of the two reflections are close-by, we should see a distinct interference pattern with valleys at some frequencies. This is the case when measuring in the forward direction. The reason that the interference pattern changes much when the measurement is repeated from the other direction could be the attenuation experienced by a wave passing over the contact fingers. When we measure from the right side,

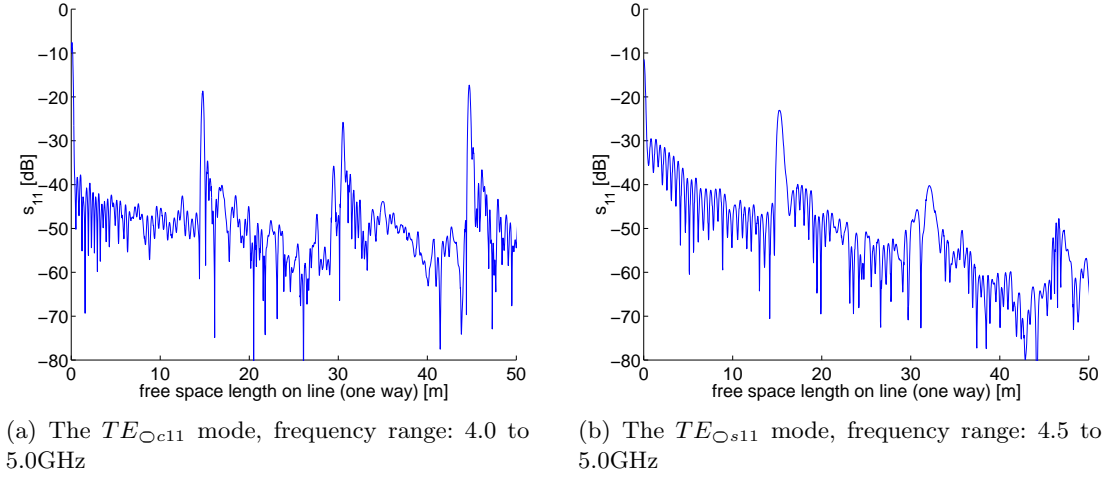


Figure 6.7: The TE modes on the test track, dispersion compensated data

the welding reflection goes back directly, while the moving contact reflection has to pass over the gap twice. As it can be assumed that the welding makes better contact than the sliding fingers, the reflection from the right should be larger initially. After having run along the contact fingers twice, its amplitude should be closer to the welding reflection's, producing a higher standing wave ratio.

On the other hand, for a wave coming from the left, the welding reflection has to pass over the contact fingers twice, its amplitude gets even smaller and therefore the standing wave ratio and the depth of the valleys observed will decrease.

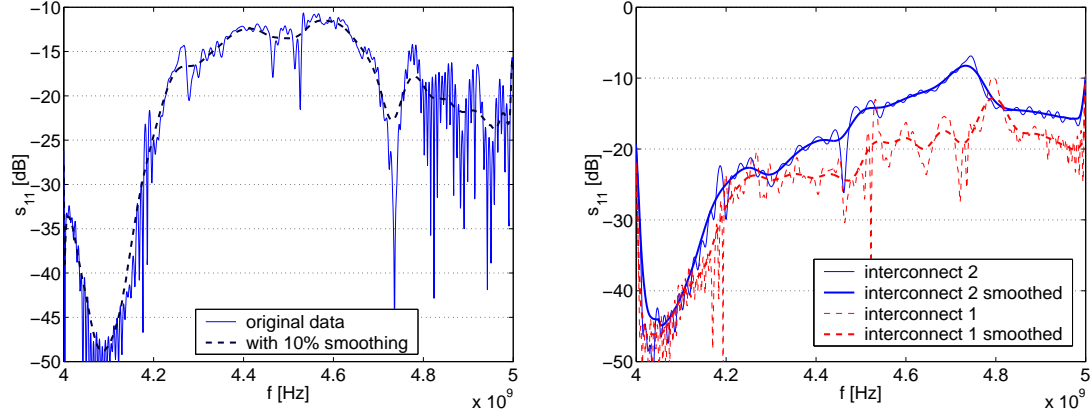
The length of the interconnects was varied between the position at ambient temperature to the operational position during one measurement session, but the results are still very preliminary.

6.4 The TE modes

The behaviour of the TE modes on the beam-pipe had to be verified in order to find out if they could not be used at all. It would be advantageous to have the possibility to switch to another mode if necessary, as this gives redundancy. As found above the TE_{Os11} mode radiates far too much. For the TE_{Oc11} mode the case is different. The dispersion compensated plots in fig. 6.7 illustrate this fact.

The measurement was performed without waveguide calibration. The reference plane was set to the waveguide adapter by doing a simple coaxial calibration on the connecting cable. This set-up was used for all the following measurements with the TE modes. The TE_{Oc11} mode propagates well, while the TE_{Os11} is heavily attenuated, a fact established already in the resonator measurements. For this reason only the TE_{Oc11} mode was examined more thoroughly.

To evaluate the effective attenuation of the TE_{Oc11} mode, the same methods as for the TM mode were applied. Fig. 6.8(a) shows the gated response of the shorted end of the test track. Since we had not done a waveguide calibration, the coupling loss of the waveguide adapter is not corrected in the VNA and true response should be higher. As we do not know exactly the frequency response of the waveguide adapter, we can only



(a) A short, seen through the 44m of the test-track

(b) The reflections of the interconnects, not compensated for line attenuation. Note that the measurement was done backwards, so interconnect 2 was closer to the VNA than interconnect 1.

Figure 6.8: The fundamental TE mode on the test track, time domain gated data

roughly estimate the amplitude shift to be 3dB. The actual attenuation does not seem to be far off from the TM mode’s.

In figure 6.8(b) the gated reflections from the interconnects are shown. Below 4.2GHz and above 4.8GHz the residues of gating have altered the traces. They are not corrected for line attenuation, so the amplitude should be at least 1.5dB higher for the red dashed traces and 3dB higher for the solid blue traces. In addition the waveguide adapter’s estimated loss of 3dB has to be kept in mind. Between 4.2 and 4.6GHz there could be a promising field of operation for the fundamental TE mode.

6.5 Mode mixing

Overmoded operation confronts us with the risk of mode conversion, leading to phantom reflections. The measurements on the test track brought us good news concerning this problem: For operation with the TM_{001} mode no sign of mode mixing was found. Neither on the network analyser nor in the dispersion compensated data any suspicious reflections were discovered. To be sure the absence of peaks from other modes was verified the following way:

Data taken with the TM mode excitation were focused for the cut-off frequencies of the other modes. For the most important interfering mode, the TE_{0c11} , the focused data is plotted in fig. 6.9(a).

No trace of any peak apart from the out-of-focus TM reflections can be found. The 2D color representation does not give a hint either. Therefore the impact of mode mixing must be more than 30dB below the level of the desired reflections with the present excitation element, a 15mm long centered axial wire. The scale of the horizontal axis is wrong for the peaks, since they do not belong to the focused mode.

The other two images in figure 6.9 show what mode mixing actually looks like. By rotating the mode launcher by some 20° with respect to optimal TE_{0s11} mode excitation, the TE_{0c11} mode appears. The TE_{0c11} mode having lower cut-off, its

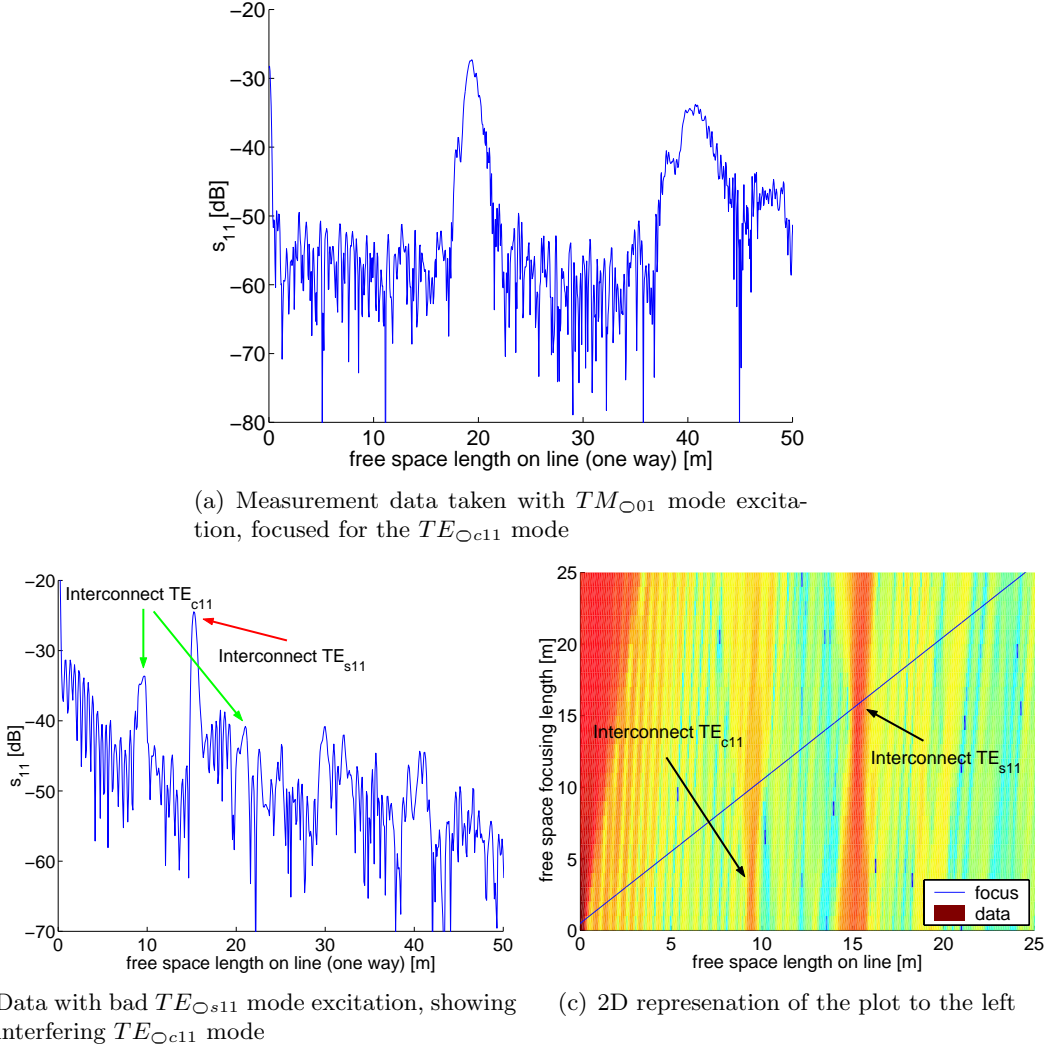


Figure 6.9: Mode mixing on the test track

group delay is smaller and therefore its peak appears earlier, at 9.5m. After the TE_{0s11} reflection from the first interconnect, even the second interconnect’s TE_{0c11} peak can be distinguished. In fig. 6.9(c) the first “bad” peak is shown. By checking the observed focusing length l_{real} as defined in fig. 5.12(b) the peak’s provenience can be verified.

6.6 Power scattering from the slots

When the time domain response of the test track was observed, another interesting phenomenon was encountered:

Between the rather large reflections from the interconnects, the amplitude should go down to the VNA’s noise level. This at least was observed for the C-band waveguide. For the beam-pipe however the response levels off close to -50dB (see fig. 6.1(a)). Where does this effect come from?

Well, what we see is that the beam-pipe is not really a good waveguide, since it is

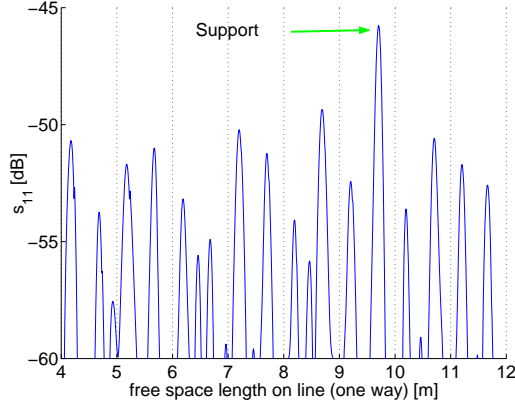
not *smooth*. There are four rows of slots, each slot having a length between 6 and 10mm. The length and position of the slots were varied to prevent resonances at wavelengths close to the slot length. The pattern is repeated every 50cm [15]. Each slot gives a little reflection, which adds up incoherently with all the others. Those tiny reflections are too small to be seen. However the blocks of 50cm length will interfere constructively for certain frequencies. Therefore we should be able to see a periodical pattern both in time and in frequency domain.

Looking closer onto the response (figure 6.10) we find a distinct periodic pattern for each mode. Especially the $TE_{\circ s11}$ and the $TM_{\circ 01}$ mode show nearly 2 ripples per meter, confirming the assumption that this effect is caused by the slots. After some attempts we eventually succeeded in finding the corresponding periodicity in the frequency domain. This posed some problems as we had to isolate a very small signal by gating. What we discovered on the way was that the supports also cause noticeable reflections (see fig. 6.10(a)) by locally deforming the waveguide. After having eliminated this error source by unfastening the supports we finally found the responses plotted in fig. 6.6. Between 5.7 and 6.6GHz 6 suspicious peaks could be identified. They correspond rather well to those expected for a periodical pattern like the slots.

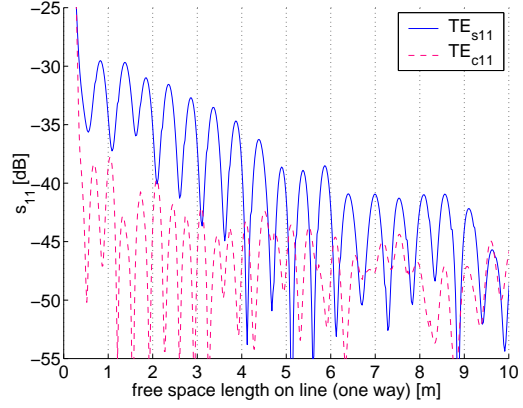
At all accounts these ripples act as a kind of background noise. They deteriorate the sensitivity of the reflectometer, and they reduce the spatial range by scattering back power. As expected the highest scattering was found for the $TE_{\circ s11}$ mode, see Figure 6.10(b). Each of the slots can be considered as a tiny impedance. In the resonator the power scattering by one single impedance cannot be measured by evaluating the quality of the resonant peaks, since it simply detunes the waveguide mode. For many little impedances however the effect is measurable, as many little reflections occur that are not in phase. Therefore they do not add up and the actual measurand, the bandwidth of the resonant peak, will be larger.

For the $TE_{\circ c11}$ mode no final statement can be made, because the periodicity does not come out clearly. Therefore it can not be excluded that the noise floor comes from bad calibration. An examination using waveguide calibration is necessary to work this out.

Integrated over 15m, the scattered power for the $TE_{\circ 01}$ mode is below the power reflected by one interconnect. Therefore scattering should not significantly reduce the spatial range.

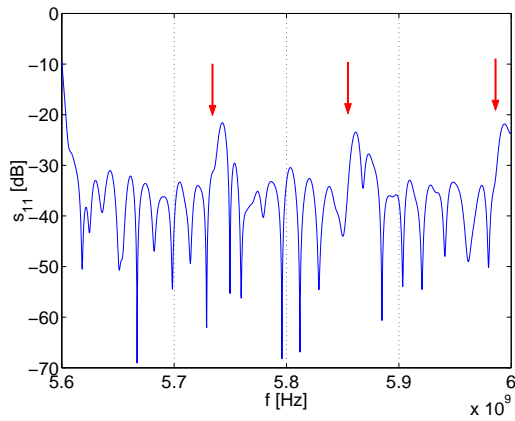


(a) The TM mode with waveguide calibration. Note that the large peak close to 10m comes from the deformation by a support

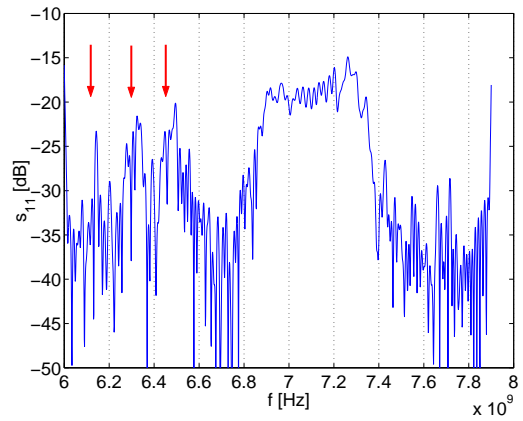


(b) The TE modes, with coax calibration up to the waveguide adapter

Figure 6.10: Zooming into the time domain response of the test track between the interconnects reveals periodic ripples coming from the periodicity of the slot pattern



(a) 1



(b) 2

Figure 6.11: The gated rippling for two different frequency ranges. The red arrows mark the location of the peaks 7 to 12 for a resonator of 49.5cm length

Chapter 7

Conclusion

The feasibility of a waveguide mode reflectometer for the LHC beam-pipe has been studied. After a start-up phase devoted to getting some experience with network analysers and waveguide calibration, the most important electrical characteristics of the beam-pipe between 4 and 8GHz have been determined in a resonator measurement. The interconnects were also examined thoroughly, for they may pose a significant problem for the reflectometer's operation. In the next step digital signal processing was applied to process the measurement data that is affected by various effects, especially dispersion. Some effects were closely examined in measurement and simulation. Finally the performance of the method was tested on the 50m test track.

The results showed that the change in the reflection profile due to a small obstacle of M4 nut size can be observed very well. However the periodicity of the slots introduces an unexpectedly high background noise. Nevertheless over short ranges (100m) it should be possible to detect and localize such small obstacles. According to current estimates the attenuation budget should allow measurements over half an arc (1250m), but the level of background noise will increase for larger ranges.

Lots of work has still to be done, especially the design of the button couplers, the refinement of the signal processing, the set-up of automated measurement routines on the network analyser and the discovery of many little tricks to make the reflectometer work well.

Appendix A

Derivation of the formula for the cut-off frequency

This derivation follows closely [10]. The complex propagation constant is defined as

$$\gamma = \alpha + j\beta \quad (\text{A.1})$$

For a cylindrical waveguide with radius a we have a cut-off frequency

$$f_c = \frac{c_0}{2\pi} \beta_\rho \quad (\text{A.2})$$

with β_ρ signifying the radial component of the propagation constant. In our actual resonator of length l we find resonances for

$$\beta_z = \frac{n\pi}{l}, \quad n = 1, 2, 3, \dots \quad (\text{A.3})$$

Using the separation condition

$$\beta_0^2 = \left(\frac{\omega}{c_0} \right)^2 = \beta_\rho^2 + \beta_z^2 \quad (\text{A.4})$$

we find for the cut-off frequency

$$f_c = \sqrt{f^2 - \left(\frac{nc_0}{2l} \right)^2}, \quad (\text{A.5})$$

depending just on the length of the resonator used, the measured resonance frequency and the index of the resonance. It does not depend on the type of waveguide used (rectangular, circular or other), as the form factor drops out. So it has to be valid also for other profiles, like the beam-pipe.

Appendix B

Characteristics of the network analysers used

For this work two network analysers were used:

- HP 8573D and
- Agilent E8358A

Their main characteristics are given the table [B.1](#):

	HP 8573D	Agilent E8358A
Frequency range	30kHz–6GHz	300kHz–9GHz
maximum number of points	1601	1601
dynamic range @6GHz ¹	105dB	118dB (133dB) ²
range of IF bandwidth	10Hz to 3kHz	1Hz to 35kHz

Table B.1: Comparison of the two network analysers used

In addition the E8358A offers some interesting features such as

- faster sweep time
- automated measurement possible
- Windows operation system
- equipped with LAN card

Appendix C

Picture gallery

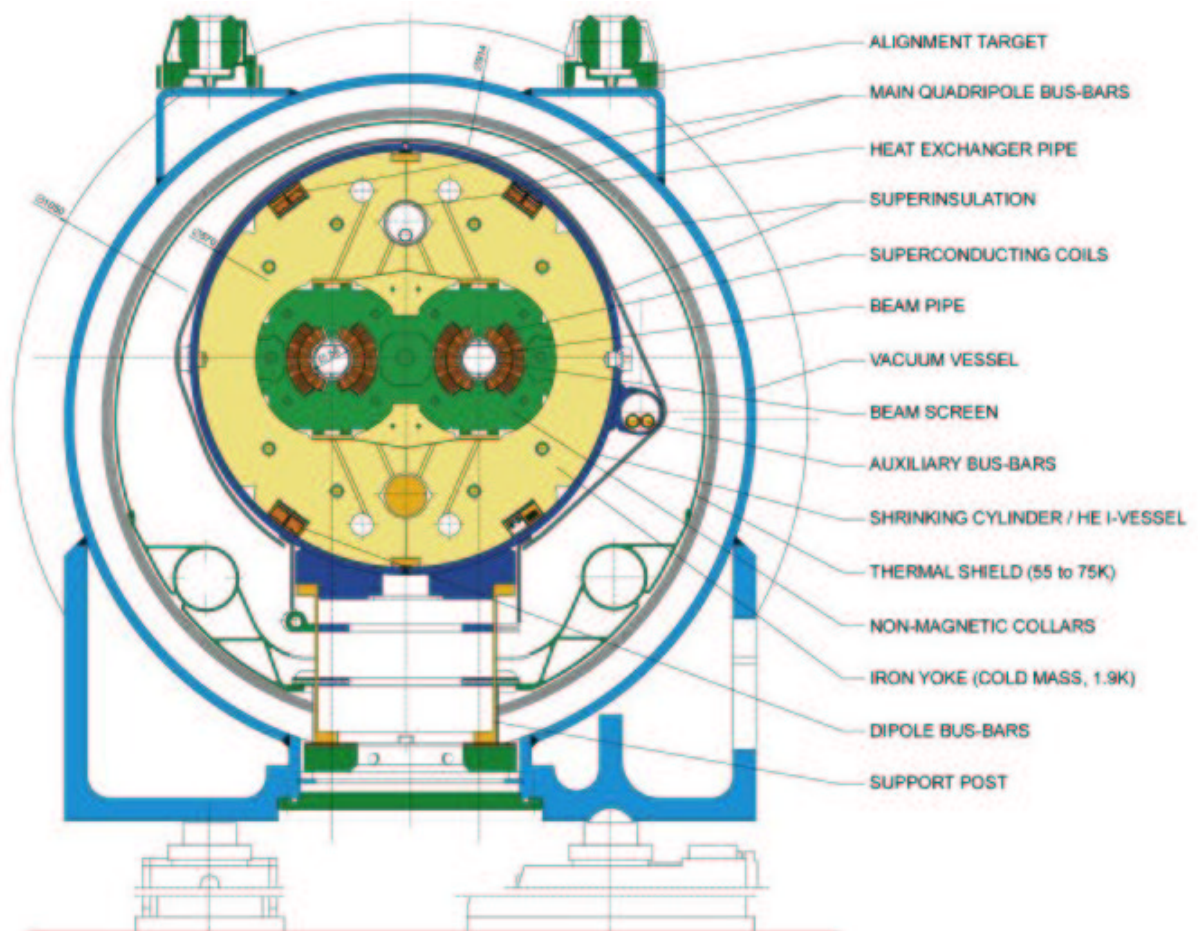
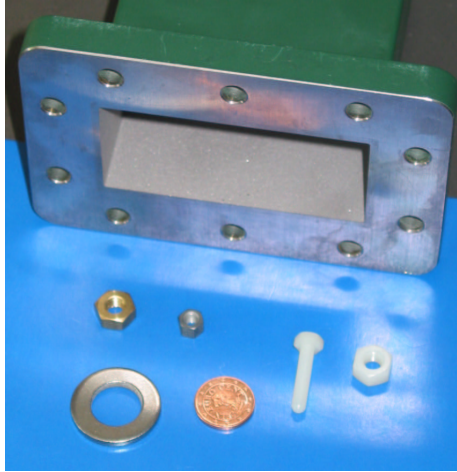
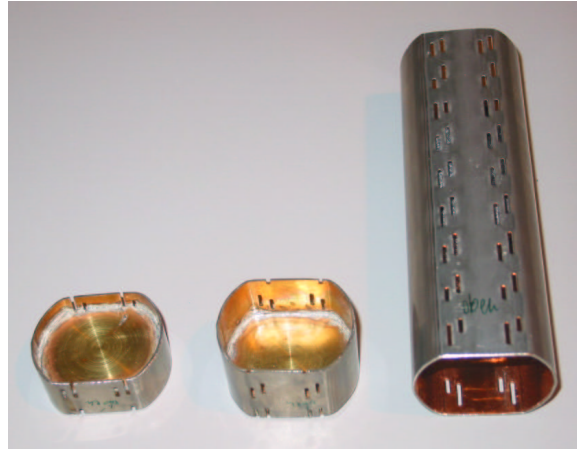


Figure C.1: View of the LHC's cross-section



(a) Some of the obstacles that were inserted into the S-band waveguide.

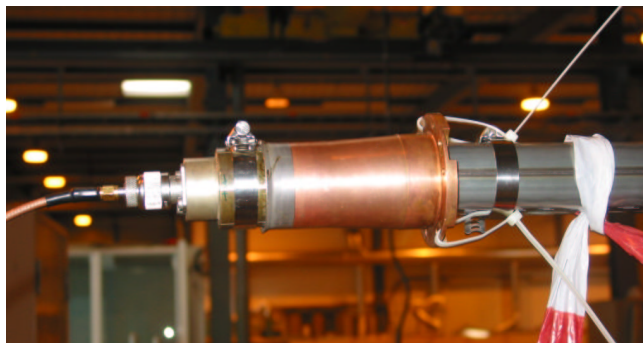


(b) The standards used for waveguide calibration on the beam-pipe.

Figure C.2:

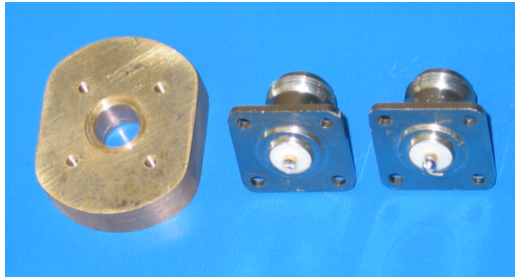


(a) A look inside reveals a TE type mode launcher.



(b) The adapter mounted on the beam-pipe on the test track.

Figure C.3: The coax-to-beam-pipe adapter.



(a) Resonator measurement: One of the brass plates that were soldered into the beam-pipe and the little mode launchers that provide very weak coupling.

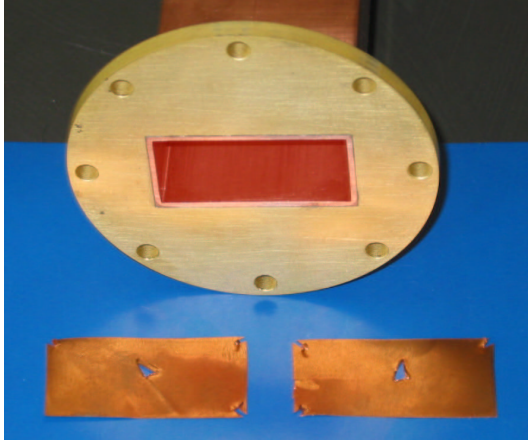


(b) Measurement in reflection mode: Larger elements for waveguide mode excitation on the test track.

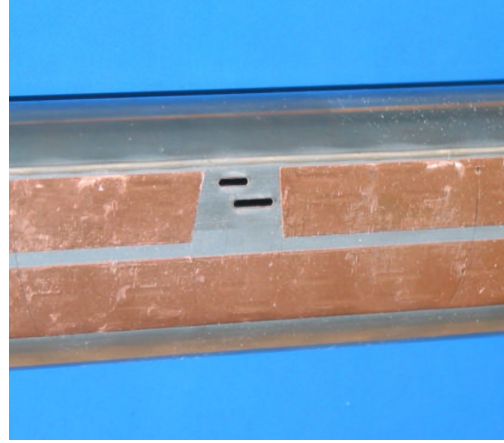
Figure C.4: Different mode launchers



Figure C.5: The two beam-pipe resonators. The slotted one was just being prepared for the radiation measurements by covering the holes with copper bands

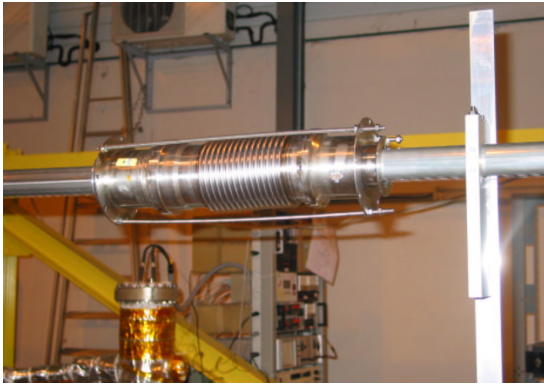


(a) A trick had to be applied to get the C-band resonator working: The coupling was done through the little holes in the copper foil. The proportions of the foils are just a little bit larger than the waveguide profile, which ensures a well-defined RF contact.



(b) The two uncovered slots for the direct radiation measurements.

Figure C.6:



(a) One of the two interconnects installed on the test track. The thread rods allow to adjust the gap length.

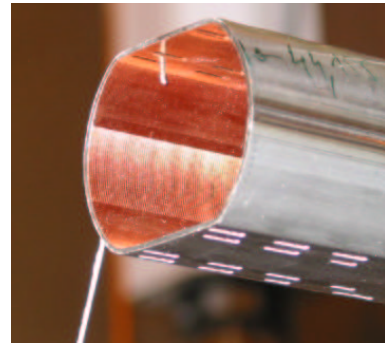


(b) LHC in the box: these BNC cables give an idea how a 700m long section of beam-pipe will behave at high frequencies.

Figure C.7: The interconnects



(a) The measurement set-up for the test track.

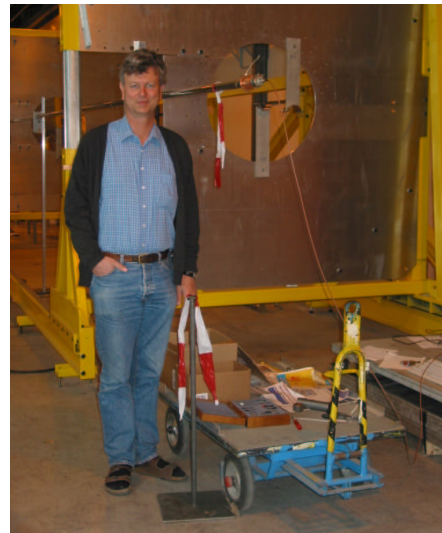


(b) The little wire that was inserted at different locations reaches just 5mm in the beam-pipe.

Figure C.8: The 50m test track



(a) The author doing measurements on the VNA...



(b) ... under the vigilant eyes of his supervisor

Figure C.9: The people involved

Bibliography

- [1] Meinke, H. and Gundlach, F. W., *Taschenbuch der Hochfrequenztechnik*, Dritte Auflage, Springer-Verlag, Berlin, 1968
- [2] Bonek, Ernst, *Wellenausbreitung 1*, Wien, 1999
- [3] Zinke, H. and Brunswig, H., *Lehrbuch der Hochfrequenztechnik*, Springer-Verlag, Berlin, 1973
- [4] Laverghetta, Thomas S., *Modern Microwave Measurements and Techniques*, Artech House, Norwood, 1988
- [5] Saad, Theodore S., *Microwave Engineers Handbook*, Volume I&II, Artech House, Dedham, 1984
- [6] *Agilent Specifying Calibration Standards for the Agilent 8510 Network Analyser*, Product Note 8510-5B
- [7] David Bello, *Network Analyser Basics*, Hewlett Packard Back to Basics Seminar, 1997
- [8] Rod Walker, *Analysis and Correction of Echo Due to Mode Conversion in WC-281 Waveguide*, IEEE Transactions on Microwave Theory and Techniques, Vol. 43, No.3, 1995
- [9] Various, *Mechanical Design Aspects of the LHC Beam Screen*, IEEE, 1998
- [10] Caspers, Fritz and Scholz, T., *Measurement of Trapped Modes in Perforated Waveguides*, CERN-PS-RF, 2000
- [11] Matthaei, George, Young, Leo and Jones, E. M. T., *Microwave Filters, Impedance-Matching Networks, and Coupling Structures*, Artech House, Dedham, 1980
- [12] Leong, Kenneth and Mazierska, Janina, *Precise Measurements of the Q Factor of Dielectric Resonators in the Transmission Mode—Accounting for Noise, Crosstalk, Delay of Uncalibrated Lines, Coupling Loss, and Coupling Reactance*, IEEE Transactions on Microwave Theory and Techniques, Vol. 50, 2002
- [13] Mostacci, Andrea, *Beam-Wall Interaction in the LHC liner*, CERN thesis-2001-014, 2001

- [14] Caspers, F., Morvillo, M., Ruggiero, F., *Surface Resistance Measurements of LHC Beam Screen Samples*, Proceedings of EPAC 2000, Vienna, 2000
- [15] Various, *Technical Spezifikation for the Manufacture of the Beam Screen Tubes for LHC Cold Arc Magnets*, LHC-VSS-CI-0001, 2000
- [16] Wilmshurst, T. H., *Signal Recovery from Noise in Electronic Instrumentation*, Institute of Physics Publishing, Bristol, 1995

Acknowledgements

This diplome project was accomplished within the framework of the CERN Technical Student Programme. I would like to express a large gratitude to my supervisor Fritz Caspers for his amiable supervision, many stimulating discussions and all the material he placed at my disposal.

My thanks also go to all the people here at CERN who helped me in various ways:

Flemming Peterson, Trevor Linnecar and Roland Garoby for supporting my project, Noël Hilleret, Juan Knaster, Hendrik and Nicolaas Kos from the AT-VAC group for the practical help by furnishing samples of beam-pipe and interconnects and setting up the test track. The mechanical parts fabricated by the RF workshop were also much appreciated. Philippe Potdevin and Magnus Eriksson were very helpful in solving all the problems with informatics that could arise during my time at CERN. Thanks also to Christian Rathjen for an interesting discussion about the impurities in the beam-pipe's copper cladding.

A very big thanks to Peter Brown, Julian Lewis, Michael Hourican and Brad Swartzwelter for reading through the draft version and trying to make it sound English.

My special thanks go to my Austrian supervisors Arpad L. Scholtz and Werner Keim from the Institute of Communications and Radio-Frequency Engineering at the Vienna University of Technology who agreed on supervising this diploma thesis.

Last but not least, thanks to my family and friends for their intellectual and emotional support which helped me during the course of my degree and this diploma project and to the girl who accepted all those long evenings I spent at the office.